Petroleum Science 23 (2026) 6979–7000

Contents lists available at ScienceDirect

Petroleum Science

journal homepage: www.keaipublishing.com/en/journals/petroleum-science

Original Paper

Thermal history reconstruction of deep diverse lithology in Tarim Basin, Northwest China

Jian Chang [a,b,c,*], Dan Li [d,**], Nan-Sheng Qiu [a,b,c], Chen-Xing Li [a,b,c]

[a] Hainan Institute of China University of Petroleum (Beijing), Sanya, 572025, Hainan, China
[b] State Key Laboratory of Petroleum Resources and Engineering, China University of Petroleum (Beijing), Beijing, 102249, China
[c] College of Geosciences, China University of Petroleum (Beijing), Beijing, 102249, China
[d] New Energy Research Institute, SINOPEC Star Petroleum Co., Ltd., Beijing, 100083, China

ARTICLE INFO

Article history:
Received 28 March 2025
Received in revised form
19 December 2025
Accepted 10 August 2026
Available online 13 August 2026

Edited by Xiu-Fang Hu

Keywords:
Deep diverse lithology
Clumped isotope thermometry
Zircon (U–Th)/He thermochronology
Thermal history
Tarim Basin

ABSTRACT

Thermal history reconstruction of deep, lithologically diverse strata (>4500 m) in sedimentary basins remains challenging because of the limited availability of reliable paleo-thermal indicators. In this study, we develop an innovative methodological framework based on independent modeling and cross-validation of multiple thermal indicators, integrating carbonate clumped isotope (Δ_{47}) thermometry, in situ U–Pb geochronology, and zircon (U–Th)/He (ZHe) thermochronology to reconstruct the thermal evolution of deep, heterogeneous strata in the Tarim Basin, Northwest China. The measured $T\Delta_{47}$ values of micrite, calcite vein, and dolomicrite samples from Cambrian–Ordovician strata in the Tabei Uplift range from 75.8 °C to 108.6 °C, while corresponding in situ U–Pb ages cluster between 463 ± 8 Ma and 495 ± 48 Ma, consistent with depositional timing. Single-grain ZHe ages from clastic rock samples range from 17.2 Ma to 472.3 Ma and are uniformly younger than their stratigraphic ages, indicating complete post-depositional He diffusion and suitability for thermal history modeling. Thermal histories reconstructed from the integrated, independently modeled thermal indicators reveal peak burial temperatures of approximately 135–210 °C since the Neoproterozoic, attributable to post-orogenic rapid sedimentation, mantle plume activity, and magmatic intrusions. Three distinct thermal evolution patterns are identified across the Tabei Uplift, leading to differential source rock maturation trajectories and hydrocarbon charging histories. The long-term low-temperature yet high-pressure conditions preserved in superdeep formations of the Tabei Uplift provide favorable conditions for liquid hydrocarbon preservation, highlighting substantial petroleum potential at great depths. Overall, this study demonstrates the robustness of a multi-indicator, cross-validated thermal reconstruction strategy and provides critical constraints on the thermal evolution of deep, diverse strata, with important implications for hydrocarbon preservation and phase behavior in superdeep reservoirs.

© 2026 The Authors. Publishing services by Elsevier B.V. on behalf of KeAi Communications Co. Ltd. This is an open access article under the CC BY license (http://creativecommons.org/licenses/by/4.0/).

1. Introduction

Deep and superdeep formations (>4500 m) in sedimentary basins—such as the Gulf of Mexico Basin, the Tarim Basin, and the Zagros Basin—have become increasingly important targets for oil and gas exploration and development (Jemison, 1979; Ma et al., 2022). Unlike most sedimentary basins, the Tarim Basin in Northwest China preserves liquid hydrocarbons at depths of ~8000 m and burial temperatures exceeding 160 °C (Yun, 2021), which challenges the conventional lower thermal limit for liquid hydrocarbon occurrence proposed by traditional petroleum theory. Because formation temperature fundamentally controls source-rock maturation and hydrocarbon phase behavior, reconstructing the thermal history of superdeep strata in the Tarim Basin is critical for explaining the persistence of liquid hydrocarbons at such depths and for constraining the effective hydrocarbon generation window.

Previous studies have primarily focused on the thermal evolution of shallow to intermediate strata in the Tarim Basin using vitrinite reflectance, apatite fission-track, and apatite or zircon

* Corresponding author.
** Corresponding author.
E-mail addresses: changjian@cup.edu.cn (J. Chang), lid9194.xxsy@sinopec.com (D. Li).

Peer review under the responsibility of China University of Petroleum (Beijing).

https://doi.org/10.1016/j.petsci.2026.08.014
1995-8226/© 2026 The Authors. Publishing services by Elsevier B.V. on behalf of KeAi Communications Co. Ltd. This is an open access article under the CC BY license (http://creativecommons.org/licenses/by/4.0/).

(U–Th)/He thermochronology (Qiu et al., 1997, 2009, 2010, 2012; Li et al., 2005, 2010, 2022; Ren et al., 2009, 2020; Chang et al., 2014, 2016, 2017). However, the thermal history of deep and superdeep strata, which experienced substantially higher temperatures, remains poorly constrained.

Reconstructing the thermal evolution of deep strata in the Tarim Basin is inherently challenging because these successions are characterized by early formation ages (mainly Neoproterozoic to Early Paleozoic), great burial depths, elevated temperatures, and a complex tectonic history. Moreover, vitrinite macerals did not appear until the Devonian, meaning that the thermal history of pre-Devonian strata can only be indirectly inferred using equivalent vitrinite reflectance converted from vitrinite-like or bitumen reflectance. Uncertainties associated with analytical precision and conversion relationships inevitably reduce the reliability of such reconstructions. In addition, the combined application of apatite fission-track and (U–Th)/He methods is primarily sensitive to temperatures of ~40–120 °C and therefore cannot effectively resolve high-temperature (>160 °C) thermal events.

The Neoproterozoic and lower Paleozoic successions of the Tarim Basin comprise diverse lithologies, including volcanic rocks, metamorphic rocks, sandstones, and carbonates (He et al., 2005; Lin et al., 2012; Xu et al., 2013; Yang et al., 2017). This lithologic diversity provides an opportunity to integrate multiple thermochronological and paleothermometric proxies. Accordingly, this study reconstructs the thermal histories of superdeep, ancient, and lithologically diverse strata in the Tarim Basin by combining zircon (U–Th)/He thermochronology, carbonate clumped isotope thermometry, and equivalent vitrinite reflectance data. This integrated, multi-proxy strategy not only offers a viable solution for pre-Devonian strata lacking primary vitrinite but also improves the robustness of thermal history reconstructions through independent modeling and cross-validation.

Zircon (U–Th)/He thermochronology is based on the accumulation of radiogenic ^{4}He produced by the alpha decay of U and Th. The effective closure temperature of zircon He diffusion increases from ~140 °C to ~220 °C with increasing radiation damage (alpha doses of 10^{16}–10^{18}; Guenthner et al., 2013), making this method particularly suitable for resolving high-temperature thermal histories. Consequently, zircon (U–Th)/He thermochronology has been widely applied to constrain the long-term thermal evolution of ancient cratonic regions, including the Qaidam Basin, Canadian Shield, Fennoscandian Shield, and Wyoming Craton (Orme et al., 2016; Powell et al., 2016; Guenthner et al., 2017; DeLucia et al., 2018; Zhong et al., 2024).

Carbonate clumped isotope thermometry is a relatively recent paleotemperature proxy that quantifies the degree of ordering between ^{13}C and ^{18}O within carbonate lattices (Eiler, 2011). The apparent equilibrium blocking temperatures of dolomite and calcite are approximately ~180 °C and ~100 °C, respectively (Henkes et al., 2014; Lloyd et al., 2018). When burial temperatures exceed these thresholds, solid-state reordering of C–O bonds occurs, allowing carbonate minerals to record peak temperatures experienced during burial. As a result, clumped isotope thermometry has been increasingly applied to reconstruct thermal histories of sedimentary basins worldwide, including those in Russia, France, the United States, Venezuela, and China (Passey and Henkes, 2012; Lloyd et al., 2018; Mangenot et al., 2019; Chang et al., 2020; Cong et al., 2021).

In this study, we systematically investigate the thermal evolution of superdeep and ancient strata in the Tarim Basin by integrating zircon (U–Th)/He thermochronology, carbonate clumped isotope thermometry, in situ carbonate U–Pb geochronology, and equivalent vitrinite reflectance. First, we examine the geochemical characteristics of carbonates, in situ U–Pb ages, and single-grain zircon He ages. Second, thermal histories since the Neoproterozoic are reconstructed using carbonate clumped isotope data modeled with solid-state reordering kinetics and zircon (U–Th)/He data modeled with the zircon radiation damage and annealing model (ZRDAAM). Finally, we evaluate the reliability of the thermal models, identify the key controls on peak burial temperatures, and discuss the implications of differential thermal evolution for hydrocarbon generation and preservation. This study provides new constraints on the thermal history of superdeep, lithologically diverse strata and offers important insights into the tectono-thermal evolution and petroleum potential of the Tarim Basin and analogous cratonic basins worldwide.

2. Geological background

The Tarim Basin in northwest China is an ancient craton basin with an area of 560,000 km^2. According to the basement relief, lithology distribution and structural characteristics, the Tarim Basin can be divided into seven tectonic units, including the Kuqa Depression, Tabei Uplift, Northern Depression, Central Uplift, Southwest Depression, Southeast Uplift, and Southeast Depression from north to south (Fig. 1(b); Yang et al., 2020a). In this study, the samples were collected from the Tabei Uplift, which is composed of the Luntai Bulge, Yingmaili Low Bulge, and Lunnan Low Bulge (Fig. 1(c); Li et al., 2012).

The unified Tarim Craton formed during the Early Neoproterozoic (1.0–0.8 Ga) along with the collisions and the amalgamation of the North and South Terranes, as was evidenced by zircon U–Pb data (Xu et al., 2013). In the Tabei Uplift, the Neoproterozoic strata consist of the mixed clastic-carbonate rocks and dolomite in the lower and upper parts, respectively (Fig. 2; Shi et al., 2018; Yang et al., 2020a). Due to the global transgression, the Tabei area evolved as a cratonic carbonate platform from the Cambrian to Late Ordovician (Li et al., 2015; Liu et al., 2018) and deposited thick dolomites and limestone. At the end of the Ordovician, the Tabei area developed into a unified uplift with the basement sloping towards the south under the influence of tectonic movements that occurred in the northern margin of the Tarim Craton (Zhu et al., 2021), which was considered as the prototype of Tabei Uplift (Meng et al., 2015). The siliceous rock, black shale, dolomite and limestone were deposited at this time and various carbonate reservoir spaces were simultaneously formed under strong karstification (Zhu et al., 2013). The significant unconformity between the Carboniferous and underlying strata in the northern Tabei Uplift and the accompanying strike-slip faults further intensified the Ordovician karstification (Fig. 2; An et al., 2009; Chen et al., 2021). Along with the spreading of the Paleo-Tethys Ocean during the Carboniferous, the Tabei Uplift deposited sandstone, mudstone, and limestone (He et al., 2005). Following the closure of the South Tianshan Ocean in the Late Permian, the Luntai Bulge on the northern flank of the Tabei Uplift occupied a structurally elevated position and experienced intense erosion, resulting in Mesozoic–Cenozoic strata directly overlying the Cambrian and Ordovician formations. In contrast, on the southern flank of the uplift (the Yingmaili Low Bulge and Lunnan Low Bulge), the Ordovician strata developed an early karst system, where erosional intensity was comparatively weaker (Fig. 2; Xiao et al., 2009). Massive geochronological datasets demonstrate that the Tarim Basin hosted Permian Large Igneous Provinces (PLIPs), characterized by intense magmatic activity during the Permian (ca. 300–269 Ma) (Xu et al., 2014; Zhang et al., 2016). It is only distributed in the western Tabei Uplift with an area of 1950 km^2 (Fig. 1(c); Meng et al., 2015). Since the Mesozoic, the Tabei Uplift has continuously received deposition except for the formation of some unconformities (Fig. 2).

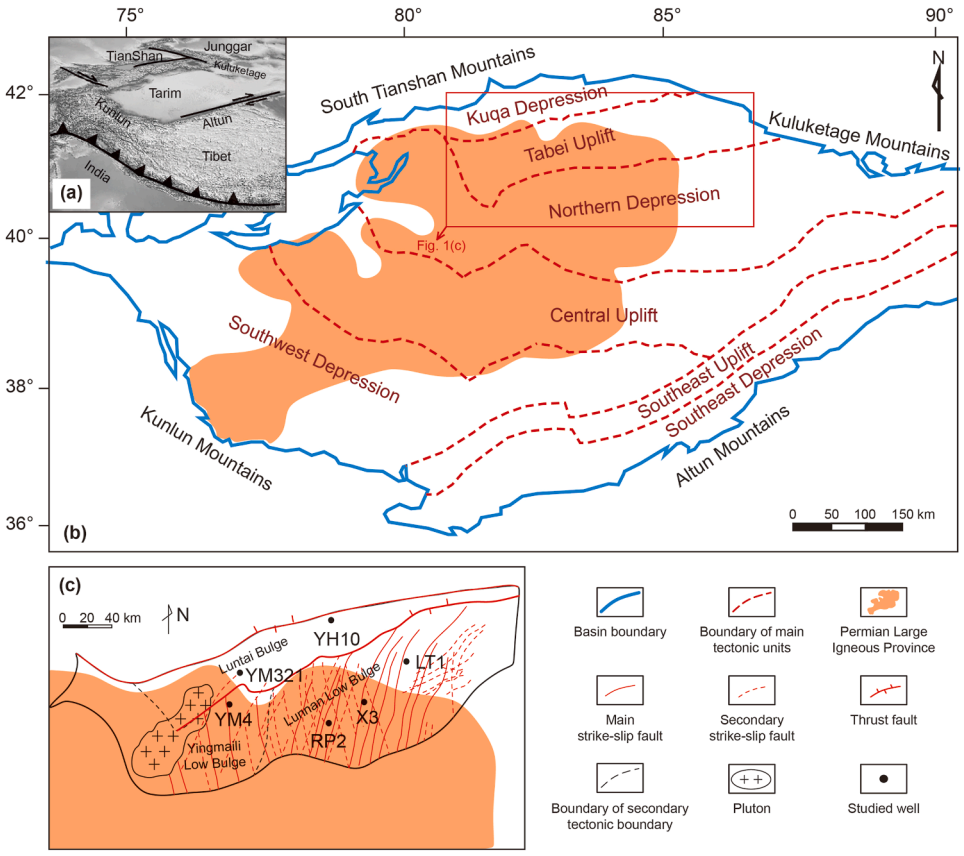


Fig. 1. **(a)** Schematic map of Central Asia showing the location of the Tarim Basin, **(b)** division of the tectonic units in the Tarim Basin showing the Permian Large Igneous Province (PLIP) and the study area (modified from Yang et al., 2013), **(c)** enlarged view of the study area showing the faults and studied wells.

Mao et al. (2014) considered that the deep oil and gas resources in the southern slope of the Tabei Uplift are primarily sourced from the Neoproterozoic–Ordovician source rocks in the Northern Depression, while that in the northern slope of the Tabei Uplift originate from the Triassic–Jurassic source rocks in the Kuqa Depression. The Lower–Middle Cambrian and Middle–Upper Ordovician source rocks across the Tabei Uplift and Northern Depression exhibit total organic carbon (TOC) contents consistently >0.5% (Fan et al., 2021; Hu et al., 2025), indicative of prolific hydrocarbon-generating potential. The deep reservoirs including the Lower Cambrian Wusonggeer Formation and the Lower–Middle Ordovician Yingshan–Yijianfang formations in the Tabei Uplift developed a lot of pores and cracks formed by dissolution and tectonism (Lü et al., 2007).

3. Samples and methods

For this study, we collected twenty carbonate samples and five sandstone samples from six wells in the Tabei Uplift, detailed information of which (including the lithology, strata, depth, and formation temperature) and location can be found in Table 1 and Fig. 1(c). The limestone and dolomite samples were subjected to the analysis of the X-ray diffraction (XRD), cathodoluminescence (CL), Δ_{47}, and in situ U–Pb experiments, while the sandstone samples were suitable for the ZHe analysis (Fig. 3 and Table S1).

3.1. X-ray diffraction (XRD) and cathodoluminescence (CL) experiments

We examined the carbonate clumped isotope of 54 aliquots from 20 carbonate samples, which were checked by XRD and CL techniques to avoid the influence of recrystallization and impurity (Huntington et al., 2011). The carbonate samples were first ground into 200-mesh powder using a mortar and pestle. For quantifying the mineral composition, the XRD experiment was carried out using a Bruker D2 Phaser diffractometer with CuK α radiations of a LynxEyeTM detector under 30 kV voltage and 10 mA intensity. The samples with calcite or dolomite contents >95% were selected for the analysis of the carbonate clumped isotope (Table S1). In addition, we analyzed the recrystallization degree of the samples based on the color and intensity of CL images (Fig. 3). We selected samples with patchy-luminescence (PL) and non-luminescence (NL) as pristine and near-pristine for clumped isotope measurements (Fig. 3).

3.2. Carbonate clumped isotope experiment

The proportions of ^{13}C–^{18}O bonds in carbonate minerals are sensitive to their growth temperatures, so the carbonate clumped isotope can be used as a quantitative paleothermometer (Eiler, 2006). The signal Δ_{47} represents the abundance of the ^{13}C–^{18}O bonds of CO_2 produced by acid digestion of the carbonate rocks (Henkes et al., 2013). $T\Delta_{47}$ means the temperature derived from the carbonate clumped isotope, which is calculated from Δ_{47} using the clumped isotope thermometer calibrations (Henkes et al., 2013, 2014). The solid-state reordering of the ^{13}C–^{18}O bonds at high-temperatures results in the variation of $T\Delta_{47}$, which makes it possible to reconstruct the thermal history of the sedimentary basins (Lloyd et al., 2018). Isotopic analyses ($\delta^{13}C$, $\delta^{18}O$, and Δ_{47}) were performed using a Thermo-Fisher MAT 253 Plus isotope ratio mass spectrometer (IRMS; Thermos Fisher Scientific Inc., USA) in the Nanjing Institute of Geology and Palaeontology, Chinese

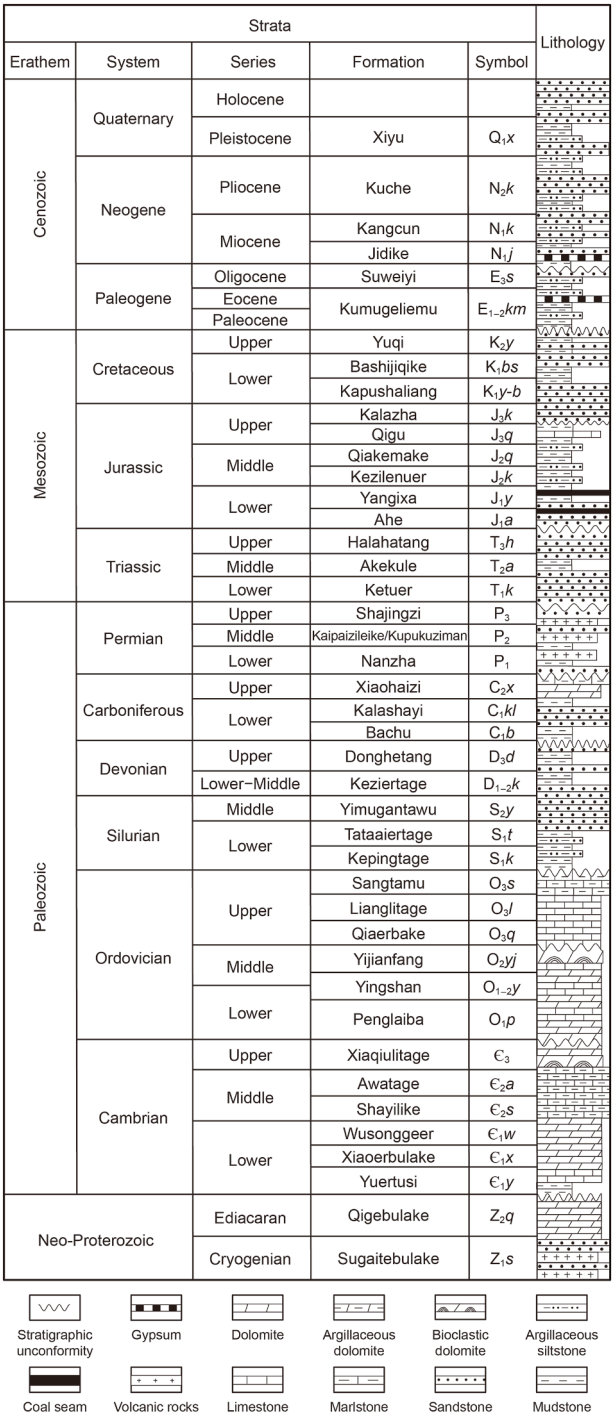


Fig. 2. Stratigraphic column of the Tabei Uplift (modified from Li et al., 2022).

Academy of Sciences, following the procedures outlined in Passey et al. (2010) and Ryb and Eiler (2018). Approximately 5–20 mg of carbonate rock powder was weighed into silver capsules for clumped isotope analysis. The IBEXII (Imperial Batch Extraction) equipment was used to produce and purify the CO_2 and measure Δ_{47} in a 105% phosphoric acid bath at an acid digestion temperature of 90 °C. To avoid the mixing of different determining compositions, the five carbonate samples were drilled using a hand Dremel with drill bits of 0.5 mm and 1.0 mm.

The obtained raw Δ_{47} was normalized by the carbon dioxide equilibrium scale (CDES) through the absolute reference frame (ARF) established by the carbonate standards ETH 1–ETH 4 (Dennis et al., 2011; Bernasconi et al., 2018). The results for the reaction temperatures of 90 °C and 70 °C were corrected to 25 °C using the acid fractionation factors (AFF) of 0.082‰ and 0.062‰, respectively (Defliese et al., 2015; Müller et al., 2017). The $\delta^{13}C$ and $\delta^{18}O$ values of these carbonate samples were shown with the Vienna Pee Dee Belemnite standard (VPDB). The apparent water oxygen isotope compositions of the precipitating waters ($\delta^{18}O_{water}$) were calculated according to Eqs. (1) and (2) proposed by O'Neil et al. (1969) for calcite and by Müller et al. (2019) for dolomite, respectively. The $\delta^{18}O$ of water was converted from the VPDB scale to the Vienna Standard Mean Ocean Water (VSMOW) scale according to Eq. (3) proposed by Kim et al. (2015).

$$1000 \ln \alpha_{water} = 2.78 \times 10^6 \times T^{-2} - 3.39 \quad (1)$$

$$1000 \ln \alpha_{water} = 2.9923 \times 10^6 \times T^{-2} - 2.3592 \quad (2)$$

$$\delta^{18}O_{VSMOW} = 1.03092 \times \delta^{18}O_{VPDB} + 30.92 \quad (3)$$

where T is temperature in Kelvin.

3.3. In situ carbonate U–Pb experiment

For the carbonate clumped isotope samples, we performed in situ U–Pb analysis by using a RESOlution SE-S155ArF-Excimer laser ablation system (LA) coupled with a Thermo Fisher iCap RQ inductively coupled plasma mass spectrometry (ICP-MS) at the Guizhou Tongwei Analytical Technology Company Limited. All the samples were cleaned with Milli-Q for 30 min and pre-ablated with the laser spot for 15 s to remove surface contaminants. For each sample, 50–80 spots were screened and measured. The laser spot diameter, laser repetition rate, and fluence were set to 120 μm, 15.21 Hz, and 6.0 J/cm^2, respectively. The measurement cycle for trace elements included 15 s of background time, 20 s of ablation time, and 15 s of washout time. The ablated portion for each sample was carried by helium and mixed with argon before entering the ICP-MS to measure the counts per second (CPS) of ^{206}Pb, ^{207}Pb, ^{208}Pb, ^{232}Th, and ^{238}U. The NIST614 glass was used as the primary reference material (RM) to correct instrument drift and to semi-quantitatively calculate U and Pb concentrations (Woodhead and Hergt, 2001). The matrix-matched calcite standard AHX-1D (recommended age of 238.2 ± 2.4 Ma) and PTKD-2 (recommended age of 153.7 ± 1.7 Ma) were used to correct for the matrix-related mass bias impacting the measured $^{238}U/^{206}Pb$ ratio (Roberts et al., 2017; Yang et al., 2021). The raw in situ U–Pb data were processed using the Iolite v. 3.64 software (University of Melbourne, Australia), and the measured in situ U–Pb ages were plotted on the Tera-Wasserburg inverse Concordia diagram using the Isoplot software (Berkeley Geochronology Center, USA).

3.4. Zircon (U–Th)/He experiment

Zircon (U–Th)/He (ZHe) thermochronology is based on ^4He produced by the alpha particle decay of U and Th radioactive isotopes. The ZHe age can be obtained by measuring the content of ^{238}U, ^{232}Th, and ^4He in the zircon minerals. In this study, the measured ZHe were performed at the $^{40}Ar/^{39}Ar$ and (U–Th)/He Laboratory, Institute of Geology and Geophysics, Chinese Academy of Sciences (IGGCAS), and the Thermochronology Laboratory, China University of Petroleum (Beijing).

Zircon grains were first obtained by standard crushing, sieving, and magnetic and density separation procedures from the sandstone samples. Under the microscope, we selected 5–8 euhedral

Table 1
Information of the samples reported in this study.

Well name	Sample No.	Lithology	Strata	Depth, m	Formation temperature, °C
Samples for X-ray diffraction, cathodoluminescence, carbonate clumped isotope, and in situ U–Pb experiments					
LT1	LT1-3	Micrite	$O_{1-2}y$	5510	135.0
	LT1-4	Dolomicrite	ϵ	8202	160.4
RP2	RP2-6	Micrite	O_2yj	6925	150.0
X3	X3-3-CV	Calcite vein	O	6200	140.0
	X3-3-M	Micrite	O	6200	140.0
YH10	YH10-11	Dolomicrite	ϵ	6212	151.0
	YH10-6	Dolomicrite	ϵ	6173	145.0
YM321	YM321-12	Dolomicrite	ϵ	5383	125.0
YM4	YM4-8	Micrite	O	5121	109.0
	YM4-9	Micrite	O	5130	117.0
Samples for zircon (U–Th)/He experiment					
LT1	LT1-5	Sandstone	Z_2q	8765–8788	165.0
RP2	RP2-5	Sandstone	S_1k	6419–6420	138.0
X3	X3-4	Sandstone	C_1	5704–5708	122.0
YM321	YM321-2	Dolomitic conglomerate	ϵ_3	5338–5339	125.0
YM4	YM4-7	Sandstone	O_1p	5068–5073	117.0

Z_2q = Qigebulake Formation; ϵ = Cambrian; ϵ_1w = Wusonggeer Formation; ϵ_3 = Xiaqiulitage Formation; O = Ordovician; O_1p = Penglaiba Formation; $O_{1-2}y$ = Yingshan Formation; O_2yj = Yijianfang Formation; S_1k = Kepingtage Formation; C_1 = Lower Carboniferous; K_1bs = Bashijiqike Formation.

zircon grains per sample with a width >60 μm. The length, width, and cone height of the selected zircon grains were measured to calculate the surface area to volume ratio to correct for alpha particle ejection and then each zircon grain was enclosed within a 1 mm × 1 mm niobium capsule (Farley et al., 1996). The concentration of ^{4}He was measured by an Alphachron MKII He Extraction and Measurement Instrument with a quadrupole mass spectrometer (QMS; Australia Scientific Instruments). The measured niobium micro vials were placed in a Teflon vial and dissolved with the known concentrations of ^{235}U, ^{230}Th, and HF solutions after the completion of ^{4}He extraction. Subsequently, the concentrations of U and Th in the zircon grains were performed by a Thermo Fisher X-Series II inductively coupled plasma-mass spectrometry (ICP-MS) instrument. The ZHe ages were processed using the IsoplotR (Vermeesch, 2018), and raw data were corrected according to the computational model proposed by Gautheron and Tassan-Got (2010).

4. Results

4.1. Stable isotope compositions

The Cambrian–Ordovician carbonate rocks in the Tabei Uplift exhibit $\delta^{13}C_{VPDB}$ values ranging from −2.60‰ to 1.03‰ with an average value of −0.62‰ and $\delta^{18}O_{VPDB}$ values with a range from −11.79‰ to −4.78‰ (an average value of −7.17‰) (Table S1). The micrite, calcite vein, and dolomicrite samples exhibit distinct $\delta^{13}C_{VPDB}$ and $\delta^{18}O_{VPDB}$ values (Fig. 4(a)). Micrite and calcite vein samples show $\delta^{18}O_{VPDB}$ values ranging from −11.79‰ to −6.61‰, exhibiting a narrower isotopic range compared to the dolomicrite samples (from −6.34‰ to −4.78‰) (Fig. 4(a)). Similarly, $\delta^{13}C_{VPDB}$ values vary between −2.60‰ and 0.40‰ in micrite and calcite vein samples, whereas dolomicrite samples display both higher maximum value (1.03‰) and a broader $\delta^{13}C_{VPDB}$ distribution (from −1.68‰ to 1.03‰). The measured $\delta^{13}C_{VPDB}$ and $\delta^{18}O_{VPDB}$ values predominantly overlap with the global Cambrian–Ordovician marine carbonate baseline (brachiopod shells and pristine fossils), indicating preservation of primary geochemical signatures in the Cambrian and Ordovician carbonate samples (Wadleigh and Veizer, 1992; Qing and Veizer, 1994; Zhang and Munnecke, 2016; Cao et al., 2020). The consistency of the isotopic data implies: (1) deposition under open-marine conditions consistent with global epeiric sea environments, and (2) limited post-depositional diagenetic alteration, as evidenced by the absence of significant recrystallization textures in petrographic analysis.

The Δ_{47} values of 20 carbonate samples range from 0.468‰ to 0.629‰ (Table S1). The $T\Delta_{47}$ values of micrite and calcite vein samples are calculated to be 54.2–126.3 °C based on the equation of Anderson et al. (2021) (Table S1). The $T\Delta_{47}$ values of the dolomite samples are calculated by the equation of Müller et al. (2019) and range from 46.8 °C to 135.3 °C (Table S1). Combined with the oxygen isotope ($\delta^{18}O_{VSMOW}$) and $T\Delta_{47}$ values, the $\delta^{18}O_{water}$ values are calculated to be from −7.22‰ to 6.30‰ for limestone and from −1.49‰ to 8.57‰ for dolomite (Fig. 4(c) and (d)). Notably, the positive correlations between $T\Delta_{47}$ and $\delta^{18}O_{water}$ values along constant $\delta^{18}O_{VSMOW}$ contours suggest that the carbonate precipitation predominantly occurred in low water–rock radio systems under relatively closed diagenetic conditions (Fig. 4(c) and (d); Eiler, 2011; Cummins et al., 2014; Veillard et al., 2019). In addition, some micrite and calcite vein samples fell off the primary trend, suggesting a distinct diagenetic process involving elevated water–rock ratios.

4.2. In situ U–Pb dating

The measured in situ U–Pb ages and more detailed information of the carbonate samples X3-3-M, X3-3-CV, YM4-9, YM321-12, YH10-6, and LT1-3 are shown in Table 2 and Fig. 5. Noted that the calcite vein sample X3-3-CV crosscuts the micrite matrix sample X3-3-M. Except for sample X3-3-CV, in situ U–Pb ages of the other five samples range from 463 ± 8 Ma to 495 ± 48 Ma, representing the deposition time (Table 2 and Fig. 5). The calcite vein sample X-3-3-CV exhibit a significantly younger age of 451 ± 3 Ma, interpreted to record a Late Ordovician tectonothermal event in the Tabei Uplift (Fig. 5(b); Cong et al., 2022). Samples X3-3-M, X3-3-CV, YM4-9, and YH10-6 display mean squared weighted deviations (MSWD) < 2.5, supporting a single-age population and isotopic closed system during diagenesis (Brooks et al., 1972; Rasbury and Cole, 2009). Despite elevated U content, sample YM321-12 shows a weak CL feature, implying that it probably did not experience intense metamorphism (Cai et al., 2009; Slater and Smith, 2012; Qiao et al., 2020). Sample LT1-3 yields an elevated MSWD of 4.9, likely reflecting post-crystallization Pb/U mobility under open-system conditions (Cong et al., 2022).

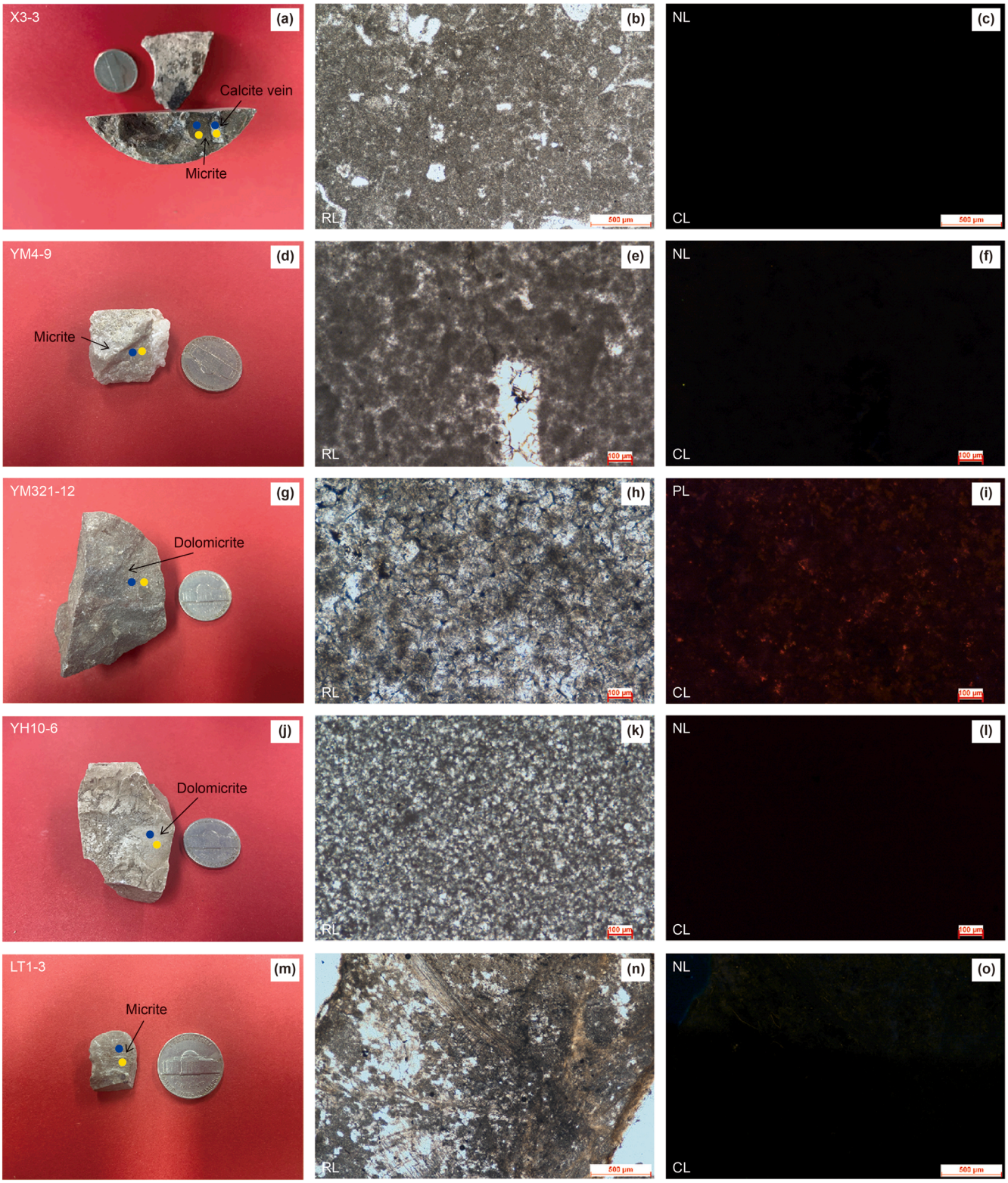


Fig. 3. Hand specimens and photomicrographs under reflected light (RL) and cathodoluminescence microscopy (CL) of carbonate rocks from the Tabei Uplift. Blue and yellow dots indicate areas for in situ U–Pb dating and clumped isotope measurements, respectively. NL = non-luminescence. The samples exhibit a non-luminescent characteristic, resulting in black images. PL = patchy-luminescence.

4.3. Zircon (U–Th)/He ages

Thirteen single-grain ZHe ages were obtained from samples YM321-2, YM4-7, X3-4, RP2-5, and LT1-5 in the Tabei Uplift (Table 3). All ZHe ages are younger than their corresponding stratigraphic ages, indicating that these zircon grains experienced the complete helium diffusion after deposition and were suitable for thermal history modeling. The Neo-Proterozoic sample LT1-5 yielded a single-grain ZHe age of 472.3 ± 2.8 Ma. The Upper Cambrian sample YM321-2 produced two ages of

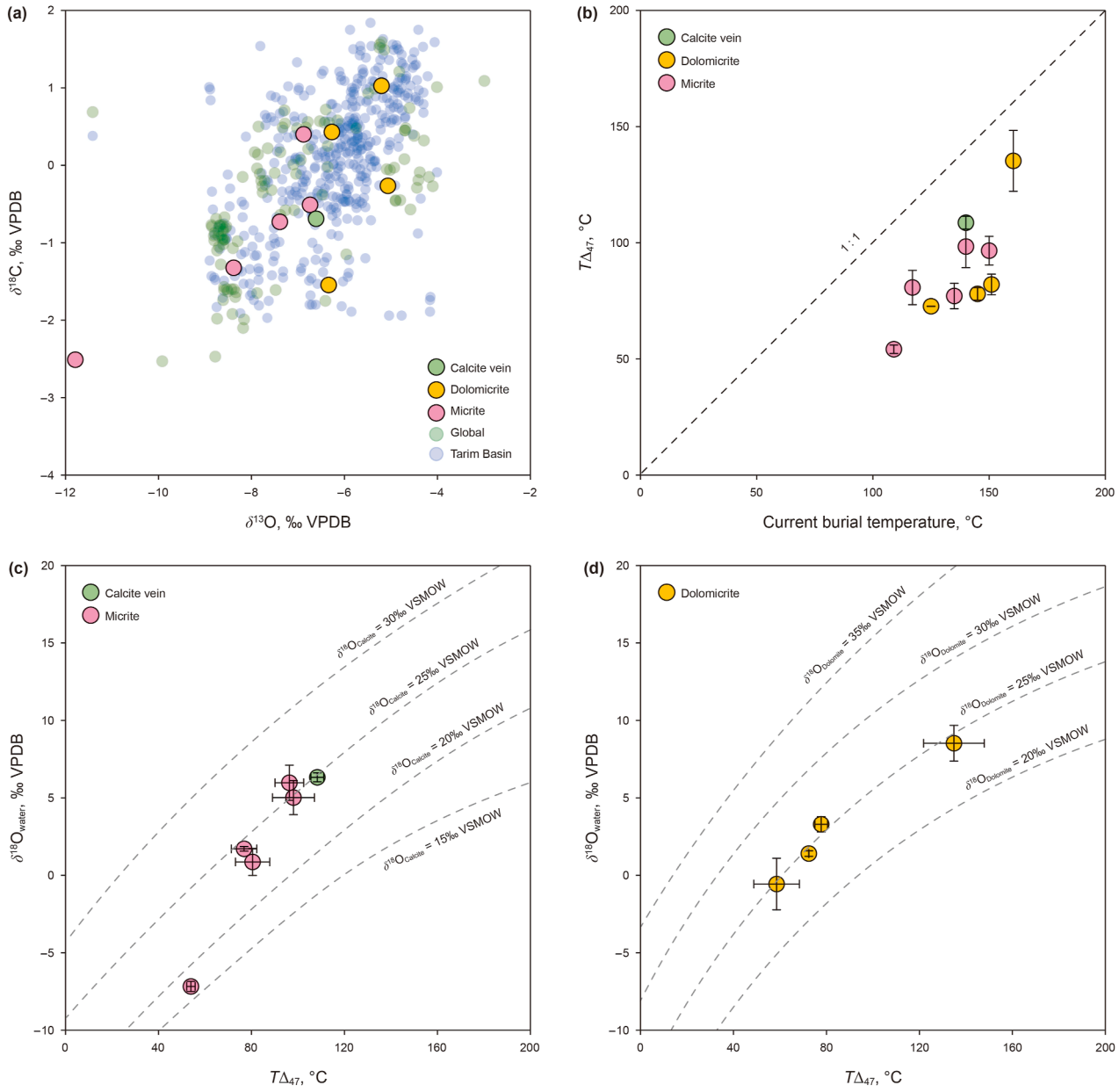


Fig. 4. **(a)** $\delta^{18}O$ vs. $\delta^{13}C$ plots of calcite vein, dolomicrite and micrite in the Tabei Uplift; **(b)** current burial temperatures vs. carbonate clumped isotope temperatures ($T\Delta_{47}$) plots of calcite vein, dolomicrite and micrite in the Tabei Uplift; **(c)** apparent water oxygen isotope compositions of the precipitating waters ($\delta^{18}O_{water}$) vs. $T\Delta_{47}$ plots of calcite vein and micrite in the Tabei Uplift; **(d)** $\delta^{18}O_{water}$ vs. $T\Delta_{47}$ plots of dolomicrite in the Tabei Uplift. The light green circles in (a) represent values from well-preserved global Cambrian–Ordovician brachiopod shells (Wadleigh and Veizer, 1992; Qing and Veizer, 1994). The light blue circles in (a) represent values from Cambrian–Ordovician unaltered fossils and micrite matrix in the Tarim Basin (Zhang and Munnecke, 2016; Cao et al., 2020). Dashed lines in Fig. 4(c) and (d) represent $\delta^{18}O_{water}$ of calcite using the equation of O'Neil and that of dolomite using the equation of Müller et al. (2019).

17.2 ± 0.1 Ma and 17.4 ± 0.1 Ma, which are much younger than other ZHe ages. Five single-grain ZHe ages from the Lower Ordovician sample YM4-7 range from 267.0 ± 0.1 Ma to 349.8 ± 4.3 Ma, exhibiting a pronounced negative correlation with the grain radius (R_s) (Fig. 6(b)). The Lower Carboniferous sample X3-4 yielded three single-grain ZHe ages of 228.1 ± 1.9 Ma, 287.9 ± 2.0 Ma, and 300.1 ± 2.3 Ma, showing a positive relationship with the R_s (Fig. 6(b)). The Lower Silurian sample RP2-5 yielded two single-grain ZHe ages of 162.6 ± 1.3 Ma and 369.2 ± 3.1 Ma.

5. Thermal history modeling

5.1. Thermal modeling parameters

In this study, the thermal histories of the samples from the wells X3, YM4, RP2, YM321, YH10, and LT1 were modeled. Thermal history inversion for borehole samples required three key parameters including the burial history, present-day temperature field and thermal indicators. The burial history was reconstructed using BasinMod 1-D software (Platte River Associates Inc., U.S.),

Table 2
Carbonate U–Pb ages, stable and clumped isotope results of carbonatite samples in the Tabei Uplift, Tarim Basin.

Sample No.	U–Pb age ± 2σ, Ma[a]	MSWD[b]	Δ_{47} ± 1SE, ‰, ARF[c]	$\delta^{13}C$ ± 1SD, ‰, VPDB[d]	$\delta^{18}O$ ± 1SD, ‰, VPDB[e]	$\delta^{18}O_{water}$ ± 1SE, ‰, VSMOW[f]	$T\Delta_{47}$ ± 1SE, °C[g]	$T\Delta_{47}$ ± 1SE, °C[h]
X3-3-CV	451 ± 3	1.9 (51)	0.504 ± 0.004	−0.69 ± 0.03	−6.61 ± 0.07	6.30 ± 0.29	108.6 ± 2.8	—
X3-3-M	463 ± 8	2.5 (56)	0.520 ± 0.014	−0.51 ± 0.12	−6.74 ± 0.12	4.99 ± 1.10	98.4 ± 9.0	—
LT1-3	474 ± 33	4.9 (38)	0.555 ± 0.010	−0.73 ± 0.10	−7.39 ± 0.94	1.68 ± 0.15	77.1 ± 5.5	—
LT1-4	—	—	0.468 ± 0.016	0.43 ± 0.06	−6.27 ± 0.01	8.57 ± 1.16	138.6 ± 14.7	135.3 ± 13.1
YM4-8	—	—	0.601 ± 0.004	−2.51 ± 0.11	−11.79 ± 0.11	−7.22 ± 0.33	54.2 ± 1.8	—
YM4-9	480 ± 74	1.8 (45)	0.549 ± 0.013	−1.32 ± 0.10	−8.38 ± 0.12	0.83 ± 0.88	80.7 ± 7.4	—
YM321-12	494 ± 15	3.2 (30)	0.568 ± 0.000	−1.55 ± 0.11	−6.34 ± 0.25	1.43 ± 0.18	70.0 ± 0.0	72.7 ± 0.0
YH10-6	495 ± 48	1.2 (47)	0.557 ± 0.005	1.03 ± 0.10	−5.20 ± 0.20	3.32 ± 0.50	75.8 ± 2.9	78.0 ± 2.7
YH10-11	—	—	0.550 ± 0.009	−0.27 ± 0.11	−5.07 ± 0.16	4.01 ± 0.48	80.1 ± 4.8	82.0 ± 4.4
RP2-6	—	—	0.504 ± 0.009	0.40 ± 0.04	−6.88 ± 0.69	5.95 ± 1.13	96.6 ± 6.2	—

[a] Uncertainties on the U–Pb ages are 2σ.
[b] MSWD reported mean squared weighted deviation. The number in bracket is the number of spot analyses made on the sample.
[c] Carbonate clumped isotope values (Δ_{47}) reported in the absolute reference frame (ARF; Dennis et al., 2011) after acid correction. Errors are 1 standard error (SE).
[d] $\delta^{13}C$ reported relative to the Vienna Pee Dee Belemnite (VPDB). Errors are 1 standard deviation (SD).
[e] $\delta^{18}O$ reported relative to the Vienna Pee Dee Belemnite (VPDB). Errors are 1 standard deviation (SD).
[f] $\delta^{18}O_{water}$ reported relative to the Vienna Standard Mean Ocean Water (VSMOW). Errors are 1 standard error (SE).
[g] $T\Delta_{47}$ was calibrated using the new Δ_{47}–temperature equation of Anderson et al. (2021).
[h] $T\Delta_{47}$ was calibrated using the dolomite Δ_{47}–temperature equation of Müller et al. (2019).

incorporating fundamental geological data and erosion amounts in the critical tectonic intervals (Table 4; Fig. 7), which were obtained based on the analysis of the wave theory (Qi and Liu, 1999; Zhang et al., 2000), R_o–depth trend (Li et al., 2010) and seismic and logging data (Wu et al., 2019). The present-day temperature field was derived from the steady-state borehole temperature profiles combined with the oil-testing temperature measurements (Table 1). Each thermal indicator possesses its own thermodynamic characteristics; therefore, when reconstructing thermal histories using multiple indicators, it is optimal to model them independently, cross-validate the results, and ultimately select the time–temperature (*t*–*T*) path that best satisfies all measured thermal indicator data. The thermal indicator comprised two datasets: (1) Δ_{47} values from samples X3-3-CV, X3-3-M, LT1-3, YM4-9, YM321-12, YH10-6, and RP2-6; and (2) single-grain ZHe ages from samples YM321-2, YM4-7, X3-4, RP2-5, YH10-7, and LT1-5.

The measured $T\Delta_{47}$ values for samples X3-3-CV, X3-3-M, LT1-3, YM4-9, YM321-12, YH10-6, and RP2-6 are lower than the corresponding present-day formation temperature (Tables 1 and 2; Fig. 4(b)), indicating that they experienced partial solid-state equilibration at the peak burial temperatures and can be used for thermal history reconstruction. In this study, thermal history modeling was carried out using the paired exchange/diffusion model of Stolper and Eiler (2015), implemented through the ClumpyCool package for Python (Python Software Foundation, USA) (Lloyd et al., 2018). The initial modeling time for each sample was set to its corresponding U–Pb age. Although some samples exhibit relatively large uncertainties in U–Pb ages (e.g., LT1-3, ±48 Ma), cathodoluminescence characteristics and stable isotope signatures indicate that they did not undergo significant late-stage diagenetic alteration; therefore, these ages remain suitable constraints for defining the initial conditions of the thermal modeling. For the micrite samples, a starting temperature of 25 °C was adopted, consistent with low-latitude Paleozoic surface seawater temperatures (Jaffrés et al., 2007; Veizer and Prokoph, 2015; Bergmann et al., 2018). For the calcite vein samples, a starting temperature of 60 °C was derived from the burial history constraints. The statistical analysis of the $T\Delta_{47}$ values from Southern China indicated that the formation temperature of the Upper Neoproterozoic dolomite was generally lower than 60 °C. Therefore, we set the starting temperature of the dolomite samples to be 40 °C (Chang et al., 2020). In addition, the precipitation timing of these samples was further constrained by in situ U–Pb data (Fig. 5). The initial time–temperature (*t*–*T*) history for each sample was calculated from the burial history without regard to other thermal anomaly effects. These models underwent iterative refinement via forward modeling until the modeled $T\Delta_{47}$ values converged with the measured data, at which point the *t*–*T* path was deemed optimal.

The thermal histories obtained from the carbonate samples were cross-validated against those of the clastic rock samples using the single-grain ZHe ages. The five single-grain ZHe ages obtained from sample YM4-7 exhibit pronounced dispersion. Previous studies have shown that such dispersion is commonly linked to the degree of accumulated radiation damage, making it difficult to interpret these ages or perform thermal modeling using the Simple Model (SM). In recent years, advances in zircon He-diffusion kinetics and forward-modeling techniques have made it possible to extract reliable thermal information from multiple single-grain ZHe ages obtained from a single sample (Guenthner et al., 2015; Powell et al., 2016). In this study, all zircon grains have *e*U values between 101.9 and 791.2 ppm, corresponding to relatively low levels of radiation damage (Fig. 6(a)). For low-damage zircon grains from ancient cratonic basins, the age-*e*U patterns simulated by the ZRDAAM and the Fanning Linear Arrhenius Model (FLAM) are highly comparable (Chang et al., 2022a). Considering this, together with the fact that ZRDAAM has been widely applied in previous ZHe-based thermal history studies, we also adopt the ZRDAAM framework in this study to model the thermal histories. This study simulated the thermal history of the sample YM4-7 by a combination of forward and inverse modeling using the ZRDAAM proposed by Guenthner et al. (2013), while other samples YM321-2, X3-4, RP2-5, YH10-7 and LT1-5 just implement the inverse modeling due to the limited ZHe ages. The measured U, Th, and He contents and single-grain ZHe ages for the sample YM4-7 were used for forward modeling with MATLAB software. Considering the inherent radiation damage and the complexity of provenance, the starting time for samples was set to be the zero-inheritance zircon He ages (depositional time and usually equal to the youngest zircon U–Pb peak age) and inheritance zircon He ages (older zircon U–Pb peak ages) (Chang et al., 2022b). The starting depositional temperature was the same as the surface temperature (14 °C). The *t*–*T* path was deemed

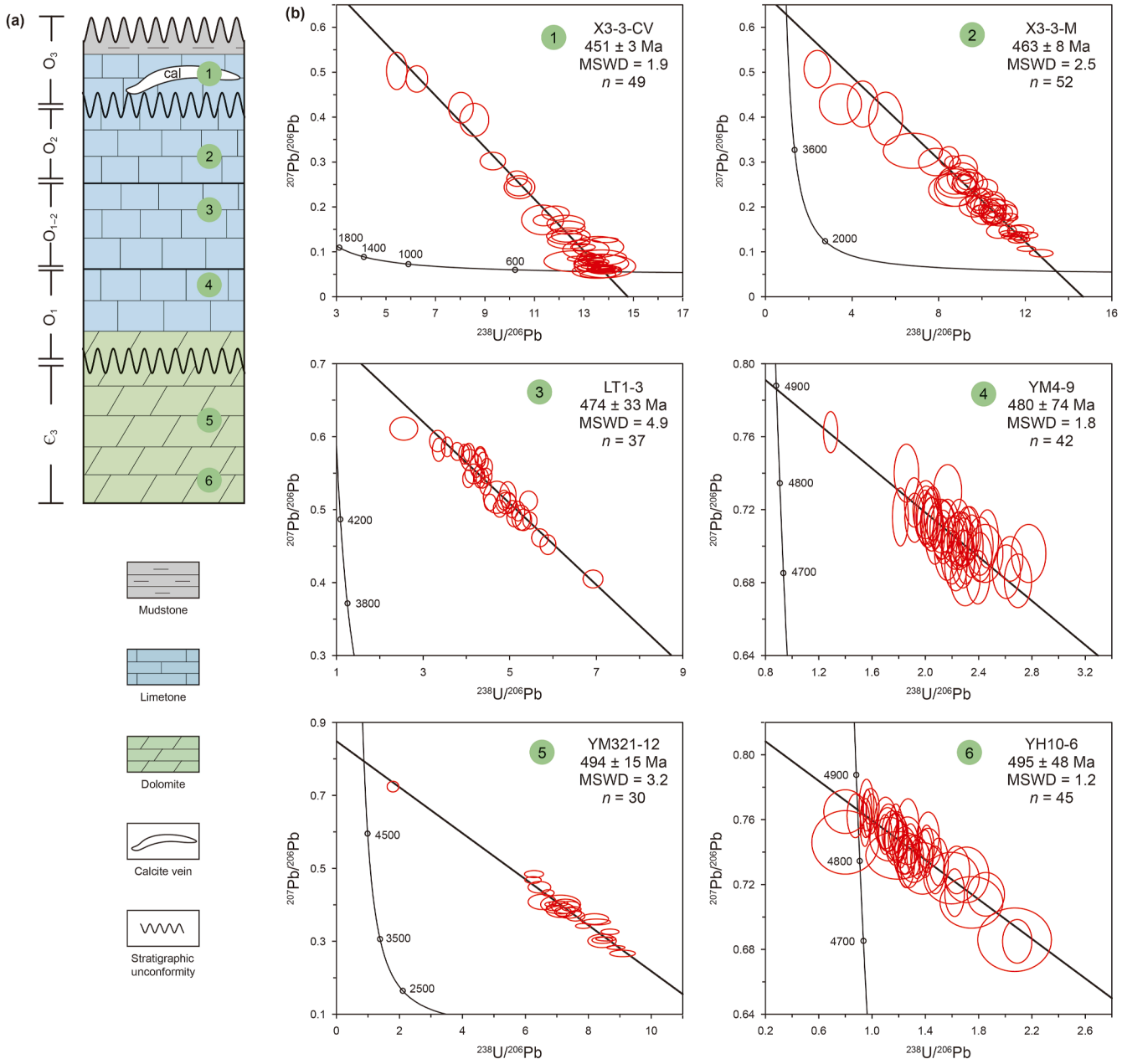


Fig. 5. **(a)** A sketch illustrates the succession of the main tectonic events and their cathodoluminescence (CL) response in the Tabei Uplift, **(b)** Tera-Wasserburg inverse Concordia diagrams showing $^{238}U/^{206}Pb$ vs. $^{207}Pb/^{206}Pb$ by in situ U–Pb dating of carbonatite samples in the Tabei Uplift. Uncertainty ellipsoids of spot analysis are plotted in red and represent 2σ uncertainties. MSWD = mean squared weighted deviation. n = the number of spot analyses.

optimal when most single-grain ZHe ages could fall into the inheritance envelope. The upper and lower boundaries of the inheritance envelope were obtained by adding and subtracting the standard deviation of the average R_s of the zircon grains, respectively. In addition, the typical single-grain ZHe ages were used for inverse modeling with the HeFTy software (Ketcham, 2005).

5.2. Early Permian thermal anomaly (samples of wells X3, YM4, and RP2)

According to the drilling data, the Well X3 area in the central Lunnan Low Bulge develops the Ordovician, Carboniferous, Permian, Triassic, Jurassic, Cretaceous, Paleogene, Neogene, and Quaternary strata (Figs. 1(b) and 7(a)). Based on the regional tectonic evolution and the unconformity distribution characteristics, the cooling events in the Middle Ordovician, Late Ordovician, Late Carboniferous, Late Permian, Late Triassic, Late Jurassic, Late Cretaceous, and Late Paleogene were set for t–T paths of the Well X3 (Fig. 8).

Under the assumption of no anomalous thermal effects in the Well X3 area, the thermal histories of samples X3-3-M (micrite) and X3-3-CV (calcite vein) were simulated with the constraint of the t–T paths (black lines in Fig. 8(a) and (b)), which were derived from the geothermal gradient and burial depth. The precipitation timing of the samples X3-3-M and X3-3-CV was set to be 463 Ma and 451 Ma based on the measured U–Pb data, respectively. The initial modeling yielded $T\Delta_{47}$ values significantly lower than the measured $T\Delta_{47}$ values, indicating insufficient peak burial

Table 3
Measured zircon (U–Th)/He data from the Tabei Uplift, Tarim Basin.

Sample No.	Stratigraphic age, Ma	Grain No.	^{4}He, ncc	Mass, ug	F_T[a]	U, ppm	Th, ppm	eU, ppm[b]	Corrected age ± 1σ, Ma	R_s, μm[c]
YM321-2	500	1	1.1	1.5	0.61	467.4	160.4	505.1	17.2 ± 0.0	35.8
		2	2.9	3.4	0.66	514.3	138.0	546.7	17.4 ± 0.0	41.4
YM4-7	480	1	27.8	2.5	0.66	407.5	224.0	460.1	267.0 ± 0.1	42.1
		2	9.5	2.2	0.74	150.4	89.4	171.4	276.7 ± 2.7	44.1
		3	22.7	2.3	0.65	332.6	229.5	386.5	281.8 ± 0.1	40.5
		4	17.4	1.8	0.71	348.0	117.2	375.6	302.9 ± 1.4	37.5
		5	20.0	1.3	0.62	461.4	130.2	492.0	349.8 ± 4.3	36.2
X3-4	350	1	52.6	4.2	0.77	412.9	153.6	449.0	228.1 ± 1.9	50.2
		2	28.4	7.2	0.82	93.4	73.1	110.6	287.9 ± 2.0	64.8
		3	54.9	4.7	0.79	258.9	241.4	315.6	300.1 ± 2.3	55.4
RP2-5	440	1	59.3	4.8	0.79	722.8	291.3	791.2	162.6 ± 1.3	55.1
		2	16.6	1.6	0.70	257.9	284.1	324.6	369.2 ± 3.1	39.7
LT1-5	590	1	12.8	2.9	0.74	78.7	98.5	101.9	472.3 ± 2.8	46.3

[a] F_T = alpha correction factor (Farley et al., 1996).
[b] eU = effective uranium concentration, calculated from the equation of Flowers et al. (2009).
[c] R_s is the radius of a sphere with an equivalent alpha ejection correction as the grain.

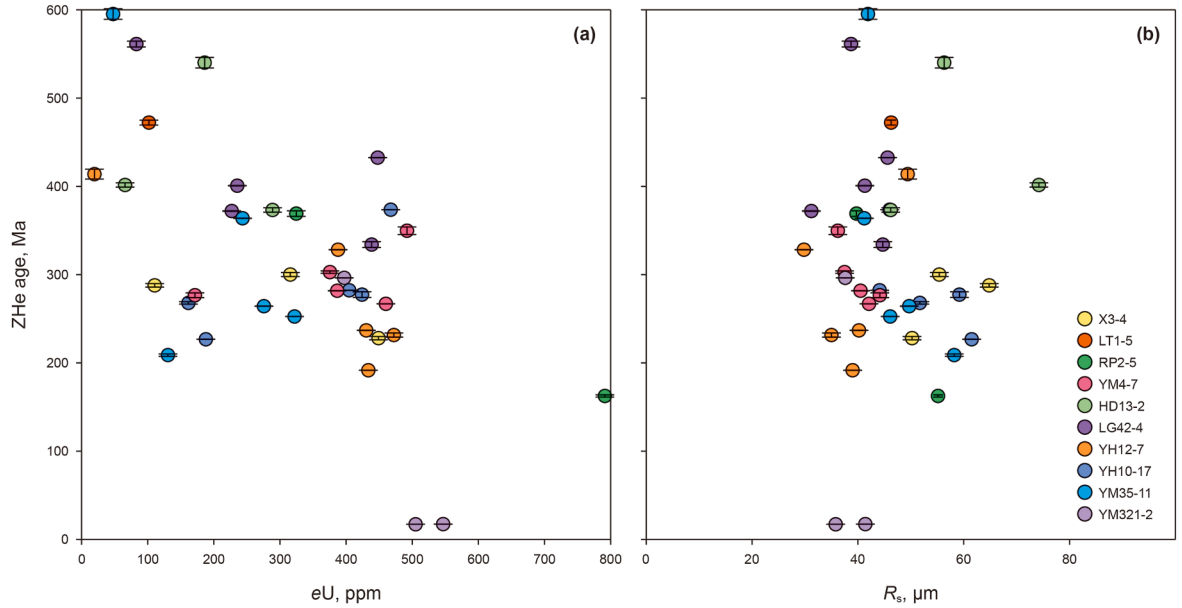


Fig. 6. Plots of effective uranium concentration (eU) **(a)** and grain radius (R_s) **(b)** vesus corrected ZHe age in the Tabei Uplift.

Table 4
Erosional amounts in the Tabei Uplift, Tarim Basin (Qi and Liu, 1999; Zhang et al., 2000; Ni et al., 2016; Wu et al., 2019; Yang et al., 2020b).

Geological periods	Erosion thickness, m					
	Well X3	Well YM4	Well YM321	Well YH10	Well RP2	Well LT1
Middle Ordovician	200	—	—	—	200	—
Late Ordovician	200	200	—		200	—
Late Silurian	500	700	900	1000	500	1000
Late Devonian	—	1200	—	—	200	—
Late Carboniferous	300	400	—	—	300	—
Late Permian	800	1200	4000	3500	800	900
Late Triassic	400	400	1000	1200	400	400
Late Jurassic	300	300	—	—	300	300
Late Cretaceous	200	200	600	600	200	200
Late Paleogene	50	50	500	500	50	80

temperatures (98 °C for the samples X3-3-M; 109 °C for the sample X3-3-CV) to drive the solid-state equilibration (Fig. 8(a) and (b)). It implied that the samples experienced much higher temperatures than normal burial temperatures in the geological time due to the magmatic activity or deep hydrothermal upwelling. Previous studies considered that the Well X3 area experienced intensive magmatic activity during the Early Permian and resulted in the regional thermal anomaly, as indicated by the vitrinite

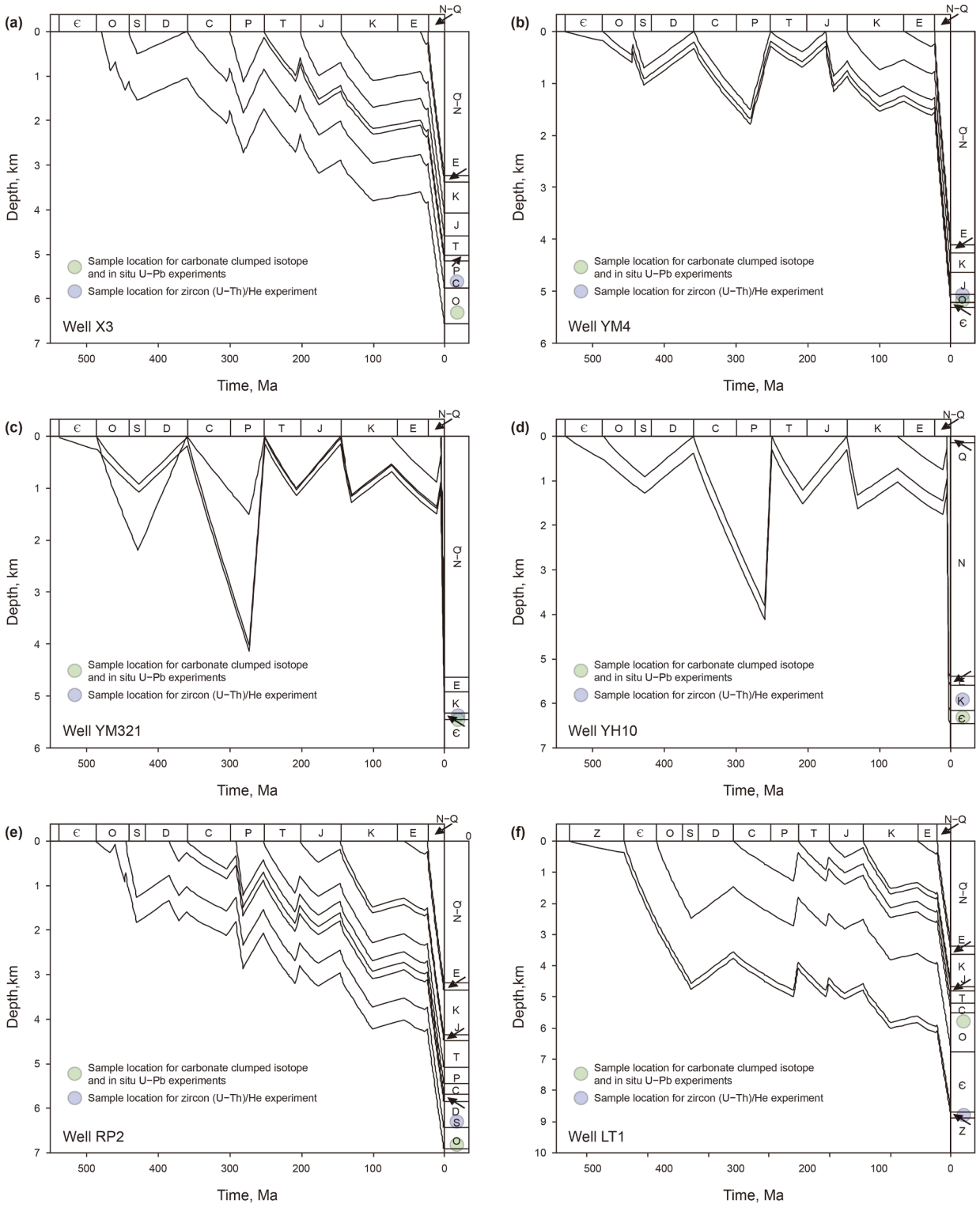


Fig. 7. Reconstructed burial histories of wells X3, YM4, YM321, YH10, RP2, and LT1, showing the residual strata and the uplift events of the Tabei Uplift, Tarim Basin. Є = Cambrian, O = Ordovician, S = Silurian, D = Devonian, C = Carboniferous, P = Permian, T = Triassic, J = Jurassic, K = Cretaceous, E = Paleogene, N = Neogene, Q = Quaternary.

reflectance (R_o) data (Li et al., 2010, 2016; Wang et al., 2010; Yang et al., 2013; Xu et al., 2014; Meng et al., 2015; Zhang et al., 2016; Cong et al., 2021). Therefore, three patterns of *t*–*T* paths with low-temperature (green lines in Fig. 8(a) and (b)), medium-temperature (red lines in Fig. 8(a) and (b)), and high-temperature (yellow lines in Fig. 8(a) and (b)) were set in the Early Permian (280 Ma) to fit the measured $T\Delta_{47}$ values of samples X3-3-M and X3-3-CV. When the modeled $T\Delta_{47}$ values were approximately equal to the measured $T\Delta_{47}$ values, samples X3-3-M and X3-3-CV experienced the peak temperatures of 200 °C and 210 °C during the Early Permian, respectively (Fig. 8(a) and (b)). In addition, the inversion result of sample X3-4 with a single-

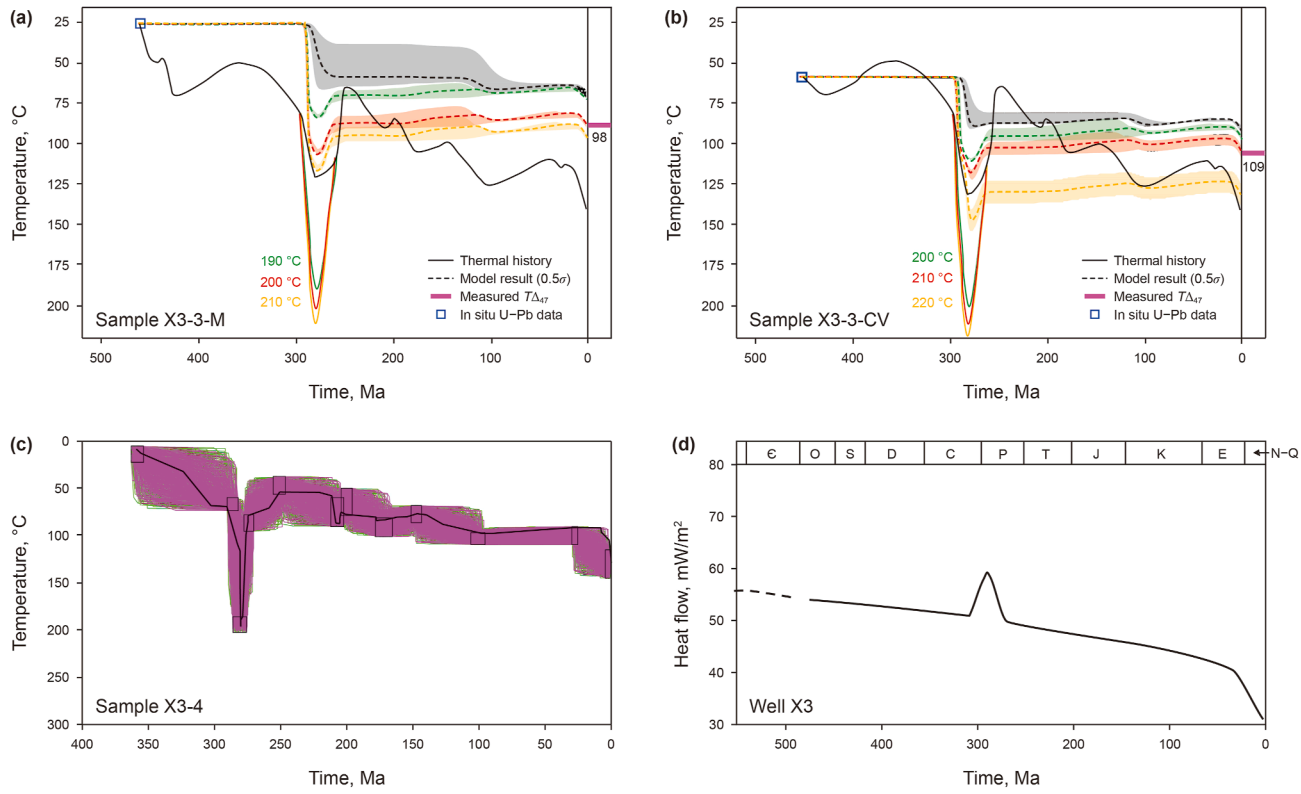


Fig. 8. Thermal history of the Well X3 in the Tabei Uplift. **(a, b)** Forward thermal history of the samples X3-3-M and X3-3-CV using carbonate clumped isotope results; purple rectangles represent the measured $T\Delta_{47}$ values; blue squares represent the precipitation timing constrained by in situ U–Pb dating; black solid lines represent the *t–T* paths calculated by the geothermal gradient and burial depth; green, red, and yellow lines represent the peak burial temperatures during the Permian with low-temperature, medium-temperature, and high-temperature, respectively; uncertainties of thermal modeling are plotted in green, red, yellow, and gray areas representing 0.5σ uncertainties. **(c)** Inverse thermal history of the sample X3-4 using zircon (U–Th)/He data; black boxes indicate *t–T* constraints, and the solid black line represents the best fitting thermal path; good paths are represented by the purple lines, whereas acceptable paths are represented by green lines. **(d)** Heat flow evolution history of the Well X3.

grain ZHe age of 228.1 ± 1.9 Ma showed a similar *t–T* path (Fig. 8(c)). The coupling forward and inversion modeling with the integration of the carbonate clumped isotope, in situ U–Pb and zircon (U–Th)/He data revealed that the heat flow in the Well X3 area decreased gradually from 55 mW/m^2 during the Cambrian to 32 mW/m^2 at the present-day, punctuated by an Early Permian thermal spike (59 mW/m^2; Fig. 8(d)). Because the Well X3 in the Tabei Uplift did not penetrate the Cambrian strata, its thickness was extrapolated through seismic data interpretation. Then the paleo-heat flow during the Cambrian was subsequently inferred from the secular trend of the reconstructed heat flow evolution (dashed line in Fig. 8(d)).

The Well YM4 in the Yingmaili Low Bulge exhibits a stratigraphic sequence encompassing the Cambrian, Ordovician, Jurassic, Cretaceous, Paleogene, Neogene, and Quaternary strata (Figs. 1(b) and 7(b)). According to the *t–T* paths obtained from the geothermal gradient and burial depth, the thermal modeling result of the sample YM4-9 shows a significant discrepancy between the calculated and measured $T\Delta_{47}$ values, suggesting that this sample experienced higher burial temperature in the geological history (black lines in Fig. 9(a)). To reconcile the measured $T\Delta_{47}$ values, we constructed three additional thermal history scenarios with varying peak burial temperatures at 280 Ma through thermal modeling (Fig. 9(a)). The simulation results identified a peak burial temperature of 200 °C at 280 Ma as the optimal *t–T* path (Fig. 9(a)). Given the proximity (60 m vertical separation) between samples YM4-9 and YM4-7, we adopted analogous post-depositional thermal paths for YM4-7 (Fig. 9(b)). According to the zircon U–Pb peak age distributions (Guo et al., 2019), we implemented three distinct thermal history simulations for YM4-7, initiating at 1800 Ma, 800 Ma, and 480 Ma to evaluate the effectiveness of inheritance envelope. Using the optimal thermal path with maximum temperature 200 °C at 280 Ma, five single-grain ZHe ages fell within the inheritance envelopes (Fig. 9(e)). This optimal *t–T* path was further validated through inverse modeling with a single-grain ZHe age of 267.0 ± 0.1 Ma (Fig. 9(c)).

Given the spatial proximity among the wells YM4, RP2, and X3, we developed three post-depositional thermal history paths for sample RP2-6 from the Well RP2 in the western Lunnan Low Bulge to reconcile measured $T\Delta_{47}$ values (Fig. S1(a)), following the method applied to samples X3-3-M and YM4-9. The optimal thermal trajectory with a peak burial temperature of 200 °C at 280 Ma demonstrates strong agreement between modeled and measured $T\Delta_{47}$ values for sample RP2-6 (Fig. S1(a)). To further constrain the thermal history revealed by the $T\Delta_{47}$ value, we conducted inverse modeling of the sample RP2-5 using a single-grain ZHe age of 369.2 ± 3.1 Ma, indicating that the Lower Silurian strata reached a peak burial temperature of 195 °C at 280 Ma (Fig. S1(b)). The 5 °C temperature difference between adjacent samples RP2-6 and RP2-5 in the Well RP2 should correlate with their 500 m vertical separation, suggesting localized thermal gradient variation.

5.3. Late Permian thermal anomaly (samples of wells YM321 and YH10)

The wells YM321 and YH10 areas in the Luntai Bulge developed the stratigraphic records of the Cambrian, Cretaceous, Paleogene,

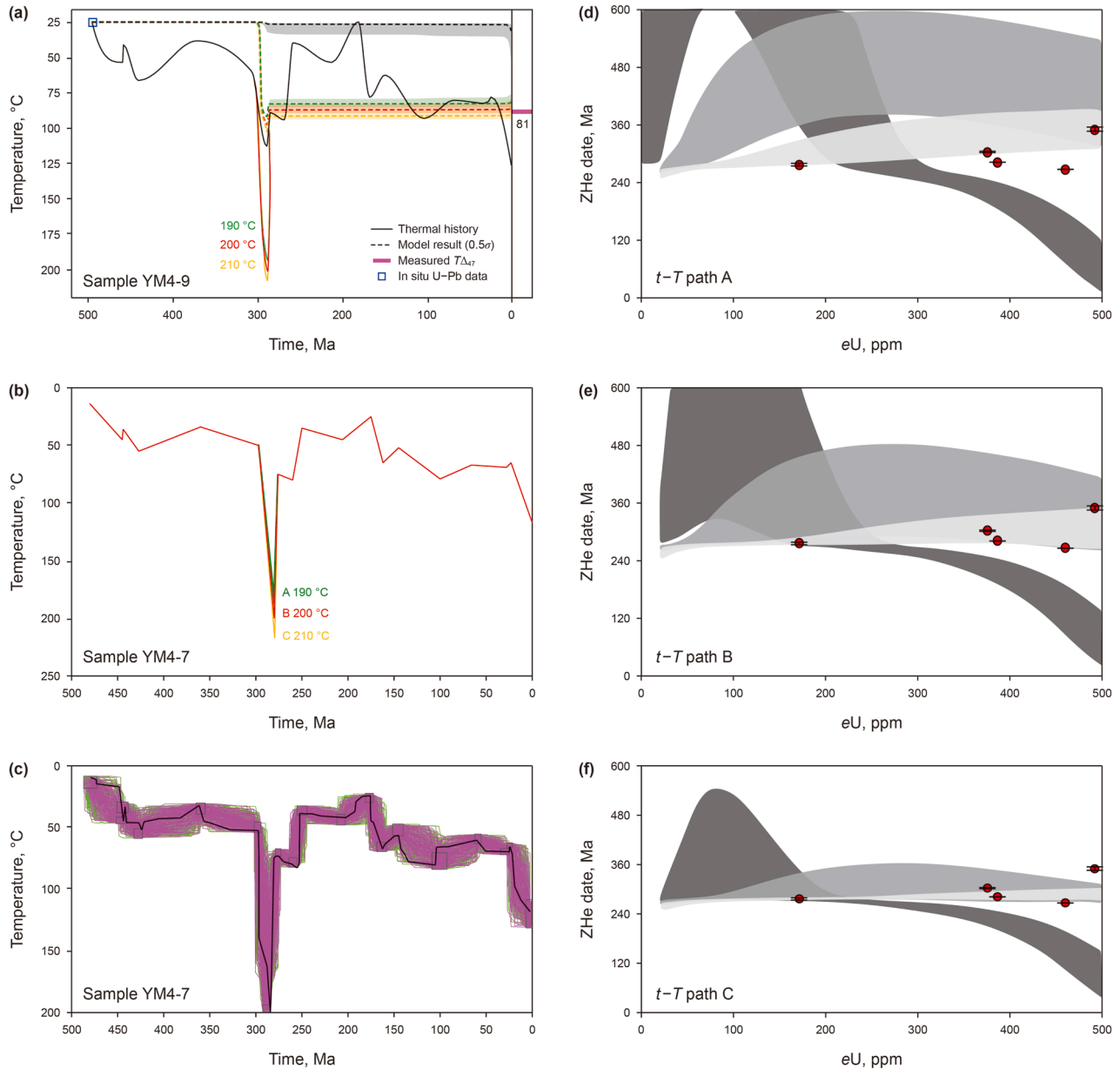


Fig. 9. Thermal histories of Well YM4 in the Tabei Uplift. **(a)** Forward thermal history of the sample YM4-9 using carbonate clumped isotope results; purple rectangles represent the measured $T\Delta_{47}$ values; blue squares represent the precipitation timing constrained by in situ U–Pb dating; black solid lines represent the *t–T* paths calculated by the geothermal gradient and burial depth, and green, red, and yellow lines represent the peak burial temperatures during the Permian with low-temperature, medium-temperature, and high-temperature, respectively; uncertainties of thermal modeling are plotted in green, red, yellow, and gray areas representing 0.5σ uncertainties. **(b)** Forward thermal history of the sample YM4-7 using zircon (U–Th)/He data. **(c)** Inverse thermal history of the sample YM4-7 using zircon (U–Th)/He data; gray boxes indicate *t–T* constraints, and the solid black line represents the best fitting thermal path; good paths are represented by the purple lines, whereas acceptable paths are represented by green lines. **(d–f)** Relationship between the measured single-grain zircon (U–Th)/He ages, and inheritance envelopes generated by three specific *t–T* paths A, B, and C in Fig. 9(b), respectively; the dark gray, medium gray and light gray areas correspond to the simulation results with the starting time 1800 Ma, 800 Ma, and 480 Ma.

Neogene, and Quaternary (Figs. 1(b), 7(c) and (d)), implying that this area experienced tectonic uplifting and exhumation events. The measured $T\Delta_{47}$ values for samples YM321-12 (73 °C) and YH10-6 (78 °C) were significantly lower than the modeled $T\Delta_{47}$ values based on the geothermal gradient and burial depth, implying that these areas experienced higher temperatures than the burial temperatures in the geological time. The published $^{40}Ar/^{39}Ar$ data of 252–267 Ma reveal that the Late Permian (~260 Ma) thermal events occurred near the wells YM321 and YH10 areas (Liu et al., 2012). Therefore, we developed three distinct thermal history scenarios with low-temperature (green lines in Figs. 10(a) and S2), medium-temperature (red lines in Figs. 10(a) and S2), and high-temperature (yellow lines in Figs. 10(a) and S2) conditions at 260 Ma for fitting the measured $T\Delta_{47}$ values of samples YM321-12 and YH10-6. Thermal simulations demonstrate that samples YM321-12 and YH10-6 reached peak temperatures of 170 °C at 260 Ma followed by rapid exhumation to ambient surface conditions (Figs. 10(a) and S2). Given the spatial proximity between samples YM321-12 and YM321-2, we applied analogous post-depositional thermal trajectories to the sample YM321-2, which was verified by the thermal modeling with a single-grain ZHe age of 296.4 ± 0.1 Ma (Fig. 10(b)).

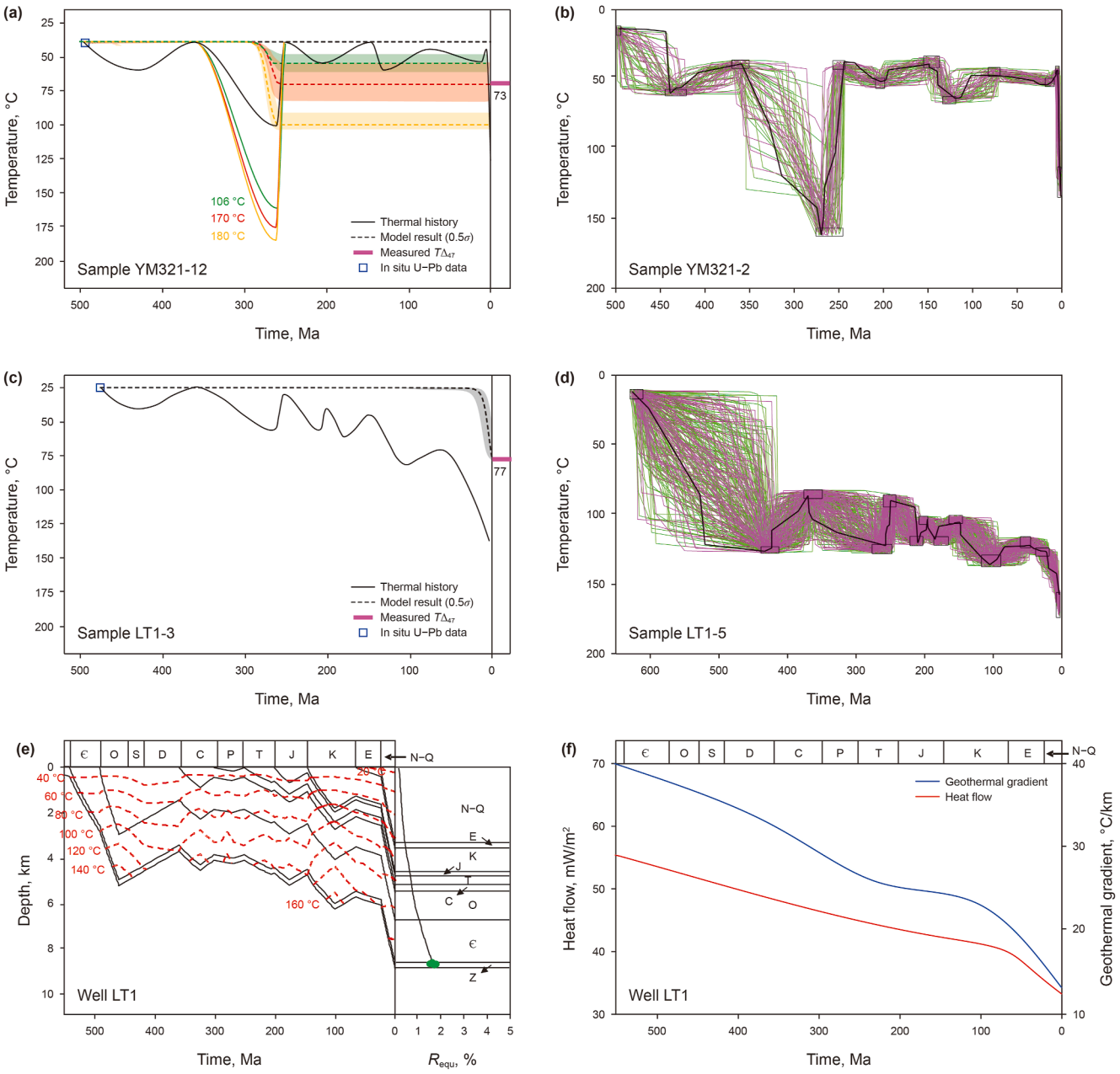


Fig. 10. Thermal histories of the wells YM321 and LT1 in the Tabei Uplift. **(a)** and **(c)** Forward thermal history of the samples YM321-12 and LT1-3 using carbonate clumped isotope results; purple rectangles represent the measured $T\Delta_{47}$ values; blue squares represent the precipitation timing constrained by in situ U–Pb dating; black solid lines represent the *t*–*T* paths calculated by the geothermal gradient and burial depth, and green, red, and yellow lines represent the peak burial temperatures during the Permian with low-temperature, medium-temperature, and high-temperature, respectively; uncertainties of thermal modeling are plotted in green, red, yellow, and gray areas representing 0.5σ uncertainties. **(b)** and **(d)** Inverse thermal history of the samples YM321-2 and LT1-5 by the zircon (U–Th)/He data. **(e)** Buried and thermal histories of Well LT1 constrained by R_{equ} data. **(f)** Heat flow and geothermal gradient evolution of Well LT1 constrained by multiple paleothermal indicators.

5.4. Tectono-thermal reconstruction of the well LT1

The Well LT1 area in the eastern Lunnan Low Bulge developed the Neo-Proterozoic, Cambrian, Ordovician, Carboniferous, Triassic, Jurassic, Cretaceous, Paleogene, Neogene, and Quaternary strata (Figs. 1(b) and 7(f)). Yang et al. (2020b) considered that the Well LT1 area experienced six stages of cooling events that occurred in the Late Silurian, Late Permian, Late Triassic, Late Jurassic, Late Cretaceous, and Late Paleogene. The burial and thermal history of the Well LT1 was preliminarily reconstructed according to the geothermal gradient, burial depth, and R_{equ} data (Fig. 10(e); Li et al., 2010; Yang et al., 2020b). Previous studies indicated that some Pb loss probably resulted in the inaccurate U–Pb ages for minerals (Rasbury and Cole, 2009; Cong et al., 2021). For the sample LT1-3, its U–Pb age of 474 ± 33 Ma is consistent with the traditional strata cognition (Fig. 5(a)), so we believe that it can serve as a constraint condition for thermal history simulation. Forward modeling of sample LT1-3 demonstrates excellent convergence between the modeled and measured $T\Delta_{47}$ values, indicating that the Lower–Middle Ordovician strata reach their maximum burial temperatures of 135 °C at present (Fig. 10(c)). Complementary inverse modeling with the single-grain ZHe age of 472.3 ± 2.8 Ma from the sample LT1-5 suggested that the Neo-Proterozoic strata reached peak temperatures of 165 °C at

present (Fig. 10(d)). Moreover, we analyzed the geothermal gradient and heat flow histories based on the thermal modeling results of the samples LT1-3 and LT1-5, which gradually decreased from 38 °C/km to 14 °C/km and from 55 mW/m^2 to 33 mW/m^2 since the Ordovician, respectively (Fig. 10(f); Li et al., 2005; Qiu et al., 2012).

6. Discussion

6.1. The uncertainty and reliability of thermal modeling

The application of carbonate clumped isotope thermometry is confronted with inherent calibration challenges due to divergent temperature sensitivities and different minerals (Bonifacie et al., 2017; Bernasconi et al., 2018; Müller et al., 2019; Anderson et al., 2021). In this study, the $T\Delta_{47}$ values were calculated and discussed using four universal Eqs. (4), (5), (6), and (7), which were established by Bonifacie et al. (2017), Petersen et al. (2019), Anderson et al. (2021), and Müller et al. (2019), respectively. The micrite and calcite vein samples yield the $T\Delta_{47}$ values of 54.2–126.3 °C based on the equation of Anderson et al. (2021), which are 7–13 °C cooler than the calculated results of Petersen et al. (2019) and 1–6 °C warmer than the calculated results of Bonifacie et al. (2017). The $T\Delta_{47}$ values of the dolomicrite samples range from 46.8 °C to 135.3 °C with the equation of Müller et al. (2019), which are 2–20 °C lower than the calibration of Petersen et al. (2019) and 2–4 °C higher than the calibration of Bonifacie et al. (2017) and Anderson et al. (2021) (Fig. 11). As shown by Fig. 11(b), the $T\Delta_{47}$ values of all the dolomite and calcite samples gradually become larger along with the increase in depth. However, at the same depth, the $T\Delta_{47}$ values of the dolomite samples are smaller than that of the calcite samples. This is probably because the reordering behavior of the dolomite is less sensitive than that of the calcite when the formation temperature is lower than ~180 °C (Henkes et al., 2014; Lloyd et al., 2018). The selection of Eqs. (6) and (7) for calculating $T\Delta_{47}$ values in our samples was based on their demonstrated superior accuracy, consistently yielding smaller uncertainties compared to alternative formulations (Fig. 11). This preference aligns with current understanding of carbonate clumped isotope systematics in natural burial environments. Moreover, Eq. (6) is derived from a newly established linear regression based on a large dataset of 41 carbonate samples spanning a broad temperature range (0.5–1100 °C) and encompassing multiple mineral types. This calibration shows strong consistency with previous studies, particularly for calcite. However, noticeable divergence arises between the regression lines of calcite and dolomite within this dataset, likely due to the limited number of dolomite samples (only four) and their relatively restricted temperature range (Anderson et al., 2021). In contrast, Eq. (7) is a mineral-specific Δ_{47}–T calibration constructed from 20 dolomite samples, rather than a unified regression across all carbonate types, and therefore provides a more accurate temperature estimation for dolomite (Müller et al., 2019). The other two calibration equations exhibit pronounced calibration offsets due to factors in early studies, including the CDES standardization scheme as well as differences in orthophosphoric acid concentration, reaction temperature, and application protocols (Anderson et al., 2021), and are therefore not adopted in this study. The paired exchange/diffusion model was specifically employed due to its capacity to incorporate more sophisticated treatment of reaction kinetics, including non-linear mechanisms that transcend the limitations of first-order approximation approaches and transient effect/equilibrium defect models. Such enhanced kinetic resolution proves particularly advantageous for thermal history

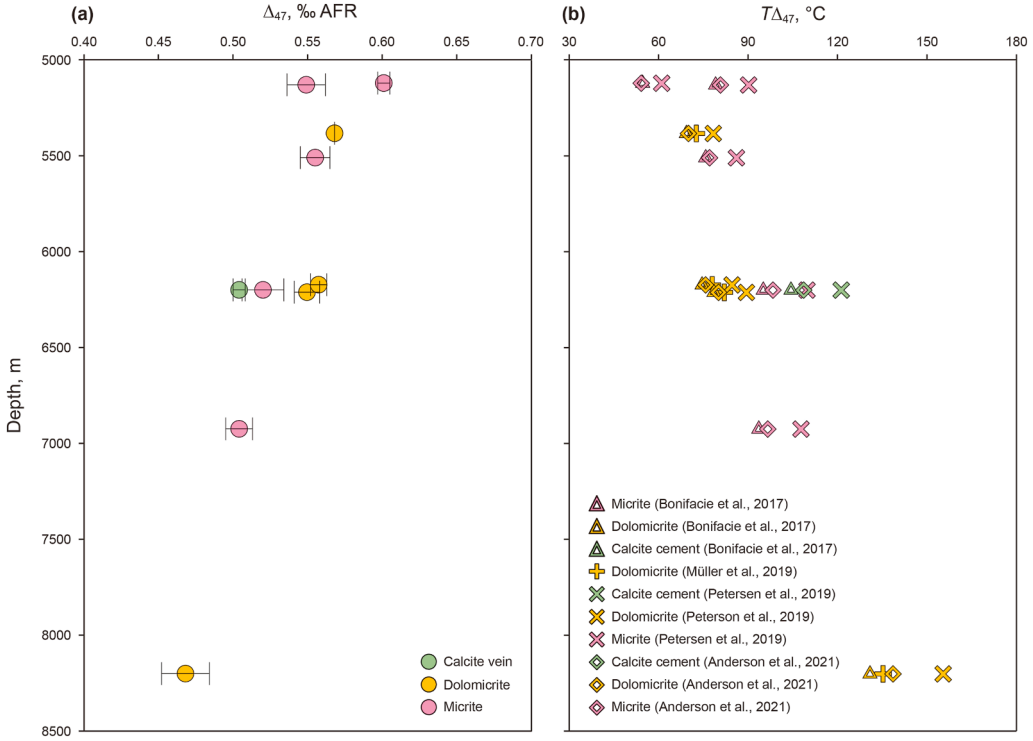


Fig. 11. Plots of carbonate clumped isotope (Δ_{47}) data **(a)** and carbonate clumped isotope temperatures ($T\Delta_{47}$) data **(b)** in relation to depth in the Tabei Uplift. The green, yellow and pink circles in panel (a) represent the calcite vein, dolomicrite and micrite. The triangle, cross, oblique cross and rhombus in panel (b) represent the calculated temperature using the Δ_{47}–temperature calibrations from Bonifacie et al. (2017) for carbonate minerals, Müller et al. (2019) for dolomite, Petersen et al. (2019) for carbonate minerals and Anderson et al. (2021) for carbonate minerals, respectively.

reconstruction in continuously subsiding sedimentary basins (Henkes et al., 2014; Stolper and Eiler, 2015; Lloyd et al., 2017; Brenner et al., 2021).

The burial history indicates that the Tabei Uplift experienced prolonged gradual subsidence within a stable depositional background (Fig. 7). Liu et al. (2020) and Cong et al. (2021) suggested that the paired exchange/diffusion model is more suitable for the platform of the Tarim Basin through comprehensive analysis of bond-reordering kinetic parameterization. Therefore, we finally selected the paired exchange/diffusion model to construct the thermal histories consistent with our observations in the Tabei Uplift.

$$\Delta_{47} = 0.0422(\pm 0.0019) \times 10^6 \times T^{-2} + 0.1262(\pm 0.0207)\ (r^2 = 0.985)$$
(90 °C acid reaction temperature, temperature calculation range 25 °C to 350 °C for carbonate minerals). (4)

$$\Delta_{47} = 0.0383\left(\pm 1.7\mathrm{E}^{-6}\right) \times 10^6 \times T^{-2} + 0.258\left(\pm 1.7\mathrm{E}^{-5}\right)\ (r^2 = 0.930)$$
(25 °C acid reaction temperature, temperature calculation range 0 °C to 800 °C for carbonate minerals). (5)

$$\Delta_{47} = 0.0391(\pm 0.0004) \times 10^6 \times T^{-2} + 0.154(\pm 0.0004)\ (r^2 = 0.970)$$
(90 °C acid reaction temperature, temperature calculation range 0.5 °C to 1, 100 °C for carbonate minerals). (6)

$$\Delta_{47} = 0.0428(\pm 0.0020) \times\ 10^6 \times T^{-2} + 0.148(\pm 0.0160)\ (r^2 = 0.864)$$
(70 °C acid reaction temperature, temperature calculation range 25 °C to 220 °C for dolomite). (7)

where T is the temperature in kelvin.

The zircon helium diffusion kinetic models include the simple model (SM), ZRDAAM, and the fanning linear Arrhenius model (FLAM) (Reiners et al., 2004; Guenthner et al., 2013; Ginster et al., 2019; Chang et al., 2022a). Compared to SM and FLAM, ZRDAAM can effectively account for the dispersity of single-grain ZHe ages caused by radiation damage and helium diffusion anisotropy and is suitable for zircons with a relatively low radiation damage dose (Powell et al., 2016; Johnson et al., 2017; Chang et al., 2022a). The single-grain ZHe ages collected from the deep and ancient strata in the Tabei Uplift were younger than the stratigraphic ages and had a low *e*U content, which is characterized by a low radiation damage dose (Table 3). Therefore, the ZRDAAM was used to study the deep and ancient thermal history of Tabei Uplift through the combination of forward and inversion modeling.

It has become an important trend to reveal ancient geological information by integrating various thermal indicators, e.g., thermal history is investigated using Δ_{47} and R_o data (Naylor et al., 2020), and the ductile–brittle transition is studied by Δ_{47} and ZHe data (Cardello et al., 2013). Considering the deep diverse lithologic characteristics in the Tabei Uplift, this paper provides more reliable thermal information under high-temperature conditions and reveals the thermal history since the Neo-Proterozoic through the mutual constraint and verification of the Δ_{47} and ZHe thermal indicators.

6.2. Thermal anomaly during the permian

The integrated thermal modeling of the $T\Delta_{47}$ and ZHe data revealed that the western Tabei Uplift except for the Well LT1 area experienced a distinct Permian thermal anomaly. This thermal perturbation appears temporally associated with three potential mechanisms: (1) sedimentary loading and subsequent tectonic uplift, (2) mantle plume activity, and (3) magmatic intrusion events. We evaluate each of the above mechanisms separately. It is important to note, however, that the anomalously high temperatures are unlikely to have been generated by any single factor, but rather by the superposition of multiple processes (Li et al., 2010, 2016; Wang et al., 2010; Cong et al., 2021).

First, we evaluated the impact of the Early Permian erosional amounts on the thermal regime in the wells X3, YM4 and RP2 areas (assuming negligible transient thermal effects) with the 1-D simulation of the BasinMod software. When the erosional amounts of the wells YM4, X3 and RP2 reached 5500 m, 4500 m, and 3000 m, respectively, the Ordovician samples collected from these wells could experience the high-temperature of 195–210 °C during the Early Permian to propel solid-state reordering and helium diffusion. However, these erosional amounts contradicted the results obtained from the wave process analysis of sedimentary basin and seismic sections (<2000 m; Table 4; Qi and Liu, 1999; Zhang et al., 2000; Ni et al., 2016; Wu et al., 2019). The wells YM321 and YH10 areas in the Luntai Bulge received sediments with a thickness of 5000 m and then suffered intense denudation in the Late Permian (Shen et al., 2007; Li et al., 2012; Yang et al., 2020b). Therefore, the calculated erosion amounts of 4000 m and 3800 m for the wells YM321 and YH10 should be reasonable (Fig. 7(c) and (d)).

Subsequently, we investigated potential thermal anomalies associated with Permian Large Igneous Provinces (PLIPs). The basalts in the Tabei Uplift are characterized by the high initial Nd isotope ratios and low heavy rare earth element values, indicating a depleted mantle source (Yang et al., 2013), while the rhyolites in the Tabei Uplift are characterized by high Nb–Ta anomalies, low $^{87}Sr/^{86}Sr(t)$ and high $\varepsilon_{Nd}(t)$ and $\varepsilon_{Hf}(t)$ values (Liu et al., 2014). According to geochemical analysis and seismic data, some studies provided several Permian mantle plume models (Liu et al., 2014; Xu et al., 2014; Li et al., 2016), which have an important effect on the surface heat flow variation in the Tabei Uplift. Mantle plume-related thermal perturbations are predominantly localized within PLIPs' core regions with peak heat flow values exceeding 90 mW/m^2 (Adeniyi et al., 2018; Feng et al., 2021; He, 2022). We calculated the Early Permian geothermal gradient near the wells RP2, X3 and YM4 as 66.4 °C/km, 69.9 °C/km, and 111.4 °C/km, respectively. It shows an increasing trend from south to north and matched the central position of the mantle plume in the northern Tarim Basin (Tian et al., 2010; Zhang et al., 2013; Li et al., 2016; Liu et al., 2020).

Furthermore, magmatic intrusion-induced thermal anomalies were evaluated. The magnitude and spatial extent of such thermal perturbations are governed by emplacement mechanisms (e.g., sills vs. dykes) and magmatic volume (Annen and Sparks, 2002; Fjeldskaar et al., 2008). In the Tabei Uplift, the limited areal extent of intrusive bodies (1950 km^2) suggests their thermal influence was restricted to proximal regions, potentially explaining localized heating anomalies observed in the YM321 well block (Stewart et al., 2005; Meng et al., 2015).

In summary, we propose that Early Permian thermal anomalies in the Yingmaili Low Bulge and western Lunnan Low Bulge were primarily driven by mantle plume activity and localized magmatic intrusions, whereas the Luntai Bulge experienced major sedimentary accumulation following Late Permian tectonic uplifting. According to heat flow histories of the typical wells in the Tabei Uplift, the thermal effect scope of the PLIPs was clarified (Fig. 12). The central–western Tabei Uplift exhibits strong PLIPs thermal anomalies, characterized by elevated Early Permian peak heat flow values of 59–75 mW/m^2 (Fig. 12(a)). Conversely, the northeastern sector shows minimal evidence of plume-related thermal imprint, retaining Paleozoic thermal characteristics with peak heat flows of 55–69 mW/m^2 that is consistent with its pre-Permian thermal regime (Fig. 12(b)).

6.3. Influence of differential tectono-thermal evolution on hydrocarbon preservation

The thermal history plays a crucial role in the maturation evolution of the source rock, oil-gas phase, and reservoir physical characteristics (Qiu et al., 2018; Ren et al., 2020). Previous studies indicated that the liquid hydrocarbon in the reservoirs would crack into gas when the reservoir temperature exceeds 150 °C (Quigley and MacKenzie, 1988; Pepper and Dodd, 1995; Waples, 2000; Tian et al., 2006; Ma, 2016; Liu et al., 2017; Li et al., 2021). The high temperature in the deep formation also improves the dissolution rate of the acid fluid, which is beneficial to the porosity increase of the carbonate reservoirs (Jiang et al., 2008; Ding et al., 2017; Peng et al., 2018). According to the three patterns of thermal histories, we systematically evaluated the hydrocarbon generation stage, oil-gas phase, and reservoir physical characteristics for the different parts of the Tabei Uplift, as synthesized in Fig. 13.

Pattern 1 is mainly distributed in the Yingmaili Low Bulge and the western Lunnan Low Bulge, as evidenced by the wells X3, RP2, and YM4 (Fig. 13). From the Ordovician to the Carboniferous, the burial temperatures of the samples X3-3-M, RP2-6, and YM4-9 slowly increased to 75 °C due to the burial diagenesis and promoted the karstification in the Yingshan, Yijianfang, and Lianglitage formations, which was characterized by the massive caves and cracks in carbonate reservoirs (Fig. 13; Su et al., 2011; Cheng et al., 2022). Meanwhile, the Middle–Upper Ordovician source rocks in the Northern Depression began to expel hydrocarbons in the Late Carboniferous, which migrated from south to north along the unconformities to the Ordovician reservoirs in the southern Tabei Uplift (Gao et al., 2012; Zhu et al., 2013). The PLIPs subsequently induced a transient thermal anomaly with peak burial temperatures reaching 190–210 °C at ~280 Ma, as constrained by fluid inclusion homogenization temperatures (Su et al., 2011; Zhu et al., 2013). This thermal pulse was followed by rapid cooling to ~80 °C during the Middle Permian (Fig. 13). Post-Permian thermal history shows gradual reheating to current subsurface temperatures below 150 °C. According to the crude oil-cracking kinetics simulation, Ma (2016) suggested that the cracking temperature of marine crude oil in the Tabei Uplift is higher than 178 °C. Therefore, the prolonged low-temperature regime (<150 °C), punctuated only by the Early Permian thermal event, has created favorable conditions for liquid hydrocarbon preservation in Lower-Middle Ordovician reservoirs in the Yingmaili Low Bulge and the western Lunnan Low Bulge (Fig. 13; Chen et al., 2015; Jia et al., 2022).

Pattern 2 is mainly distributed in the Luntai Bulge (e.g., wells YM321 and YH10; Fig. 13). From the Cambrian to the Middle-Late Permian (Fig. 13), burial diagenesis gradually elevated formation temperatures of the samples YM321-12, YM321-2, and YH10-6 to 165–170 °C. The Late Permian exhumation event resulted in direct overlying of Cambrian strata by Lower Cretaceous Kapushaliang Group, forming the buried hill structures and causing abrupt reduction of the formation temperature to surface condition (Fig. 13; Lü et al., 2007; Li et al., 2012). Subsequently, the formation temperatures of these samples slowly heated to 70–100 °C from the Triassic to Paleogene, which promoted the development of dissolved caves and cracks in dolomite and provided the basis for late hydrocarbon accumulation (Fig. 13; Han et al., 2018). Since the Neogene, the formation temperatures of these samples heated rapidly to 125–145 °C, remaining below the threshold for substantial crude oil cracking (Fig. 13). Meanwhile, the Lower–Middle Cambrian reservoir situated 150–200 m below the weathering crust received two distinct hydrocarbon charges derived from Triassic–Jurassic source rocks in the Kuqa Depression (Fig. 13; Zhang et al., 2010b; Liu et al., 2015; Wang, 2019).

Pattern 3 is mainly distributed in the Well LT1 area in the Lunnan Low Bulge (Fig. 13). The Neo-Proterozoic and Cambrian

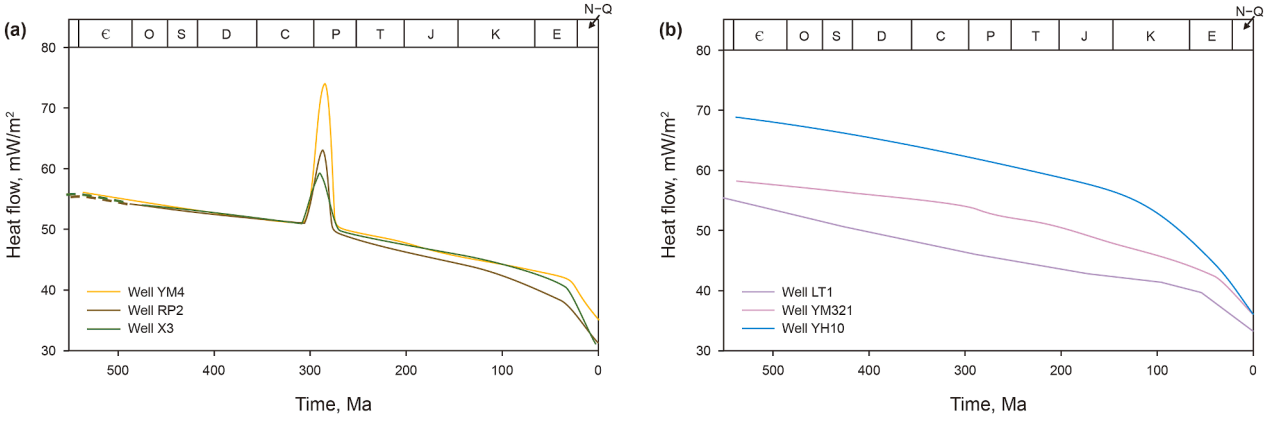


Fig. 12. Thermal history of heat flow in representative wells of the Tabei Uplift. **(a)** Central–western Tabei Uplift, **(b)** northeastern Tabei Uplift.

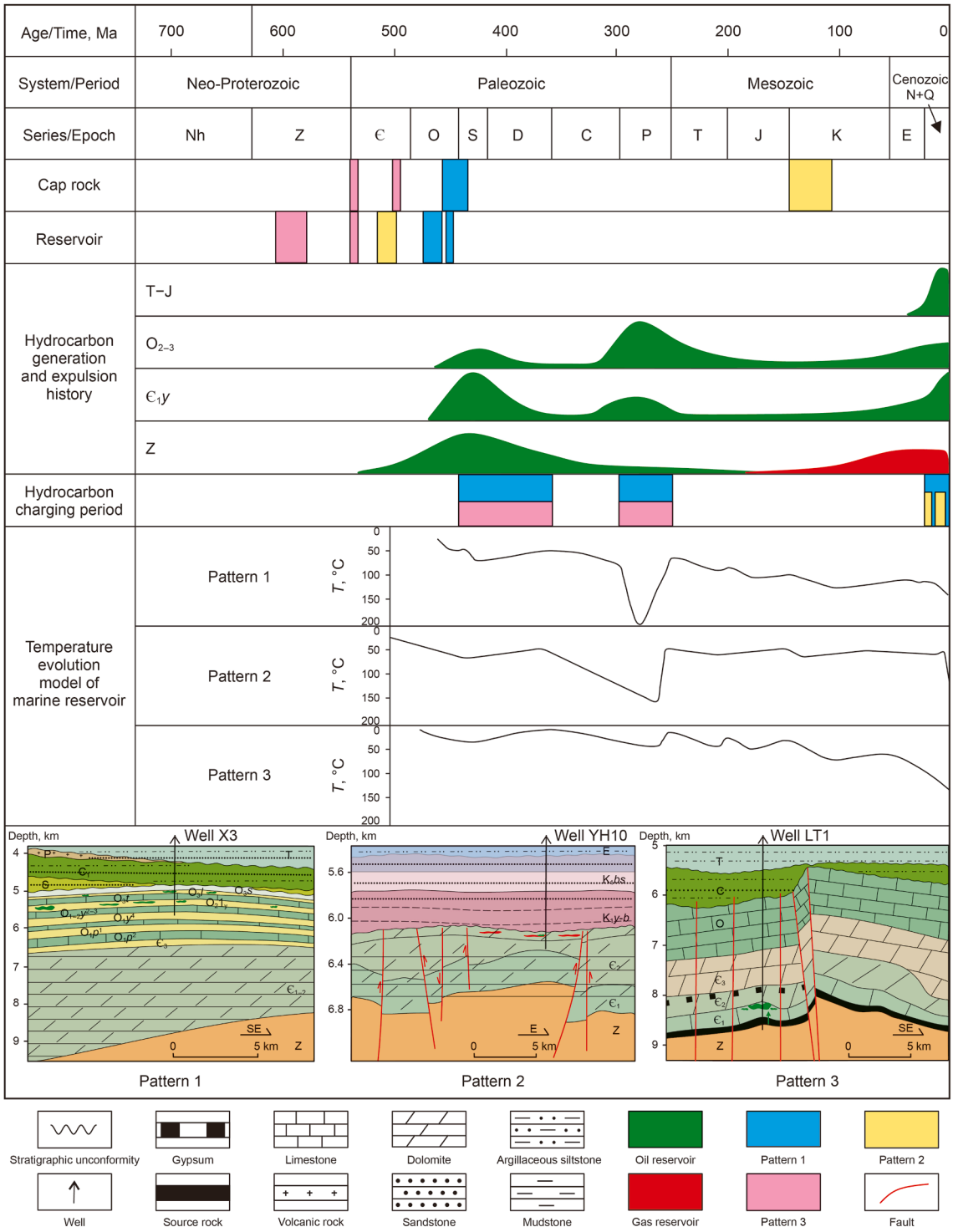


Fig. 13. Influence of differential tectono-thermal evolution on hydrocarbon preservation in the Tabei Uplift. The profile maps were modified from Su et al. (2011), Zhang et al. (2010a), and Zhu et al. (2021), respectively. A higher-resolution profile map is provided in Fig. S3. Є = Cambrian, O = Ordovician, S = Silurian, D = Devonian, C = Carboniferous, P = Permian, T = Triassic, J = Jurassic, K = Cretaceous, E = Paleogene, N = Neogene, Q = Quaternary.

strata maintained a progressive temperature increment to 100–140 °C in the Mesozoic along with the deposition, which was conducive to the preservation of primary pores (Fig. 10; Chang et al., 2021). Cenozoic rapid subsidence led the Lower Cambrian Wusonggeer Formation and the Neo-Proterozoic Qigebulake Formation to reach 165 °C and 180 °C, respectively, which are the current maximum burial temperatures (Fig. 10). Differential thermal maturation between the Lower Cambrian Yuertusi Formation

and Neoproterozoic source rocks resulted in the charge of oil and gas reservoirs in Wusonggeer and Qigebulake formations, respectively (Gu et al., 2019; Zhu et al., 2021; Sun et al., 2022).

7. Conclusions

This study employed carbonate clumped isotope thermometry and zircon (U–Th)/He thermochronology to reconstruct the thermal histories of the deep diverse lithology in the Tabei Uplift, Tarim Basin. The clumped isotope temperatures ranged from 46.8 °C to 135.3 °C, which experienced partial solid-state equilibration at peak temperatures. The single-grain ZHe ages ranged from 17.2 Ma to 472.3 Ma with an apparent dispersion, indicating that they were suitable for thermal history modeling. The combination of the carbonate clumped isotope and zircon (U–Th)/He methods effectively constrained the peak burial temperatures (135–210 °C) experienced by the samples, which were related to the huge sedimentation after the uplift, mantle plume activity, and intrusive rocks. Finally, we provide three thermal evolution patterns in the Tabei Uplift, which resulted in the differential maturation of the source rocks and hydrocarbon preservation. The integration of the carbonate clumped isotope, in situ U–Pb, and zircon (U–Th)/He methods indicates that it has the potential to become an emerging method for studying the thermal history of superdeep diverse strata in sedimentary basins.

CRediT authorship contribution statement

Jian Chang: Writing – review & editing, Writing – original draft, Software, Methodology, Funding acquisition, Formal analysis, Data curation, Conceptualization. **Dan Li:** Writing – original draft, Software, Formal analysis, Data curation. **Nan-Sheng Qiu:** Supervision, Project administration, Methodology. **Chen-Xing Li:** Software, Data curation.

Data availability

Data will be made available on request.

Declaration of competing interest

The authors declared no potential conflict of interest with respect to the research, authorship, and/or publication of this article.

Acknowledgements

This work was granted by the National Natural Science Foundation of China (No. 42272135 and U24B6001).

Supplementary data

Supplementary data to this article can be found online at https://doi.org/10.1016/j.petsci.2026.08.014.

References

Adeniyi, E.O., Ossa Ossa, F., Kramers, J.D., et al., 2018. Cause and timing of the thermal over-maturation of hydrocarbon source rocks of the Ecca Group (Main Karoo Basin, South Africa). Mar. Petrol. Geol. 91, 480–500. https://doi.org/10.1016/j.marpetgeo.2018.01.033.

Anderson, N.T., Kelson, J.R., Kele, S., et al., 2021. A unified clumped isotope thermometer calibration (0.5–1,100 °C) using carbonate-based standardization. Geophys. Res. Lett. 48, e2020GL092069. https://doi.org/10.1029/2020GL092069.

An, H.T., Li, H.Y., Wang, J.Z., et al., 2009. Tectonic evolution and its controlling on oil and gas accumulation in the northern Tarim Basin. Geotectonica Metallog 33 (1), 142–147. https://doi.org/10.3969/j.issn.1001-1552.2009.01.019.

Annen, C., Sparks, R.S.J., 2002. Effects of repetitive emplacement of basaltic intrusions on thermal evolution and melt generation in the crust. Earth Planet Sci. Lett. 203 (3–4), 937–955. https://doi.org/10.1016/S0012-821X(02)00929-9.

Bergmann, K.D., Finnegan, S., Creel, R., et al., 2018. A paired apatite and calcite clumped isotope thermometry approach to estimating Cambro–Ordovician seawater temperatures and isotopic composition. Geochem. Cosmochim. Acta 224, 18–41. https://doi.org/10.1016/j.gca.2017.11.015.

Bernasconi, S.M., Müller, I.A., Bergmann, K.D., et al., 2018. Reducing uncertainties in carbonate clumped isotope analysis through consistent carbonate-based standardization. G-cubed 19 (9), 2895–2914. https://doi.org/10.1029/2017GC007385.

Bonifacie, M., Calmels, D., Eiler, J.M., et al., 2017. Calibration of the dolomite clumped isotope thermometer from 25 to 350 °C, and implications for a universal calibration for all (Ca, Mg, Fe)CO_3 carbonates. Geochem. Cosmochim. Acta 200, 255–279. https://doi.org/10.1016/j.gca.2016.11.028.

Brenner, D.C., Passey, B.H., Holder, R.M., et al., 2021. Clumped-isotope geothermometry and carbonate U–Pb geochronology of the Alta stock metamorphic aureole, Utah, USA: Insights on the kinetics of metamorphism in carbonates. G-cubed 22, e2020GC009283. https://doi.org/10.1029/2020GC009238.

Brooks, C., Hart, S.R., Wendt, I., 1972. Realistic use of two-error regression treatments as applied to rubidium-strontium data. Rev. Geophys. 10 (2), 551–577. https://doi.org/10.1029/RG010i002p00551.

Cai, C.F., Li, K.K., Li, B., et al., 2009. Geochemical characteristics and origins of fracture- and vug-fillings of the Ordovician in Tahe oilfield, Tarm Basin. Acta Pet. Sin. 25 (10), 2399–2404 (in Chinese).

Cao, Z.C., Lu, Q.H., Gu, Y., et al., 2020. Characteristics of Ordovician reservoirs in Shunbei 1 and 5 fault zones, Tarim Basin. Oil Gas Geol 41 (5), 975–984 (in Chinese). https://doi.org/10.11743/ogg20200508.

Cardello, G., Mancktelow, N.S., Bernasconi, S.M., et al., 2013. Carbonate deformation during exhumation through the ductile-brittle transition: Insights from (U–Th)/He thermochrometry. Stable and clumped-isotopes. American Geophysical Union, Fall Meeting. T43F–2717.

Chang, B., Li, C., Liu, D., et al., 2020. Massive formation of early diagenetic dolomite in the Ediacaran Ocean: Constraints on the "dolomite problem.". Proc Natl Acad Sci USA 117 (25), 14005–14014. https://doi.org/10.1073/pnas.1916673117.

Chang, J., Brown, R.W., Yuan, W., et al., 2014. Mesozoic cooling history of the "Bachu Uplift" in the Tarim Basin, China: Constraints from zircon fission-track thermochronology. Radiat. Meas. 67, 5–14. https://doi.org/10.1016/j.radmeas.2014.05.019.

Chang, J., Qiu, N.S., Li, C.X., et al., 2022a. Zircon He diffusion kinetics models and its implications on the thermal history reconstruction of the ancient strata in the craton basins, China. Chin. J. Geophys. 65 (2), 711–725 (in Chinese).

Chang, J., Qiu, N.S., Song, X.Y., et al., 2016. Multiple cooling episodes in the Central Tarim (Northwest China) revealed by apatite fission track analysis and vitrinite reflectance data. Int. J. Earth Sci. 105 (4), 1257–1272. https://doi.org/10.1007/s00531-015-1242-7.

Chang, J., Tian, Y., Qiu, N., 2017. Mid-Late Miocene deformation of the northern Kuq a fold-and-thrust belt (southern Chinese tian Shan): An apatite (U–Th-Sm)/He study. Tectonophysics 694, 101–113. https://doi.org/10.1016/j.tecto.2016.12.003.

Chang, J., Yang, X., Qiu, N.S., et al., 2022b. Zircon (U–Th)/He thermochronology and thermal evolution of the Tarim Basin, western China. J. Asian Earth Sci. 230, 105210. https://doi.org/10.1016/j.jseaes.2022.105210.

Chang, Q.H., Zhu, G.Y., Ruan, Z., et al., 2021. Thermodynamics and kinetics model of fluid-rock interaction in carbonate-evaporite paragenesis and its application in Cambrian reservoir in Tabei area, Tarim Basin. Nat. Gas Geosci. 32 (10), 1474–1488 (in Chinese). https://doi.org/10.11764/j.issn.1672-1926.2021.04.012.

Chen, J.J., He, D.F., Sun, F.Y., et al., 2021. Framework evolution of north Tarim paleouplift from the late Ordovician to Middle Devonian. Oil Gas Geol. 42 (2), 285–298. https://doi.org/10.11743/ogg20210203 (in Chinese).

Chen, S.M., Hou, M.C., Fang, Q.F., et al., 2015. Hydrocarbon accumulation and enrichment rule of Ordovician in Yingmai-2 area, northern uplift of Tarim Basin. Lit. Res. 27 (6), 64–71. https://doi.org/10.3969/j.issn.1673-8926.2015.06.009 (in Chinese).

Cheng, H.L., Wei, J.F., Cheng, Z.Y., 2022. Study on sedimentary facies and reservoir characteristics of Paleogene sandstone in Yingmaili Block, Tarim Basin. Geofluids 2022, 1445395. https://doi.org/10.1155/2022/1445395.

Cong, F.Y., Tian, J.Q., Hao, F., et al., 2021. A thermal pulse induced by a Permian mantle plume in the Tarim Basin, Northwest China: Constraints from clumped isotope thermometry and in situ calcite U–Pb dating. J. Geophys. Res. Solid Earth 126 (4), e2020JB020636. https://doi.org/10.1029/2020JB020636.

Cong, F.Y., Tian, J.Q., Hao, F., et al., 2022. Calcite U–Pb ages constrain petroleum migration pathways in tectonic complex basins. Geology 50 (6), 644–649. https://doi.org/10.1130/G49750.1.

Cummins, R.C., Finnegan, S., Fike, D.A., et al., 2014. Carbonate clumped isotope constraints on Silurian ocean temperature and seawater $\delta^{18}O$. Geochem. Cosmochim. Acta 140, 241–258. https://doi.org/10.1016/j.gca.2014.05.024.

Defliese, W.F., Hren, M.T., Lohmann, K.C., 2015. Compositional and temperature effects of phosphoric acid fractionation on Δ47 analysis and implications for discrepant calibrations. Chem. Geol. 396, 51–60. https://doi.org/10.1016/j.chemgeo.2014.12.018.

DeLucia, M.S., Guenthner, W.R., Marshak, S., et al., 2018. Thermochronology links denudation of the Great Unconformity surface to the supercontinent cycle and snowball Earth. Geology 46 (2), 167–170. https://doi.org/10.1130/G39525.1.
Dennis, K.J., Affek, H.P., Passey, B.H., et al., 2011. Defining an absolute reference frame for 'clumped' isotope studies of CO_2. Geochem. Cosmochim. Acta 75 (22), 7117–7131. https://doi.org/10.1016/j.gca.2011.09.025.
Ding, Q., He, Z.L., Wo, Y.J., et al., 2017. Factors controlling carbonate rock dissolution under high temperature and pressure. Oil Gas Geol. 38 (4), 784–791. https://doi.org/10.11743/ogg20170415 (in Chinese).
Eiler, J.M., 2006. 'Clumped' isotope geochemistry. Geochem. Cosmochim. Acta 70 (18), A156. https://doi.org/10.1016/j.gca.2006.06.1379.
Eiler, J.M., 2011. Paleoclimate reconstruction using carbonate clumped isotope thermometry. Quat. Sci. Rev. 30 (25–26), 3575–3588. https://doi.org/10.1016/j.quascirev.2011.09.001.
Fan, Q.H., Xiao, Z.Y., Zhang, H.Z., et al., 2021. Characteristics and distribution of the Lower Cambrian source rocks in the Northern Depression, Tarim Basin. Geochimica 50 (3), 251–260. https://doi.org/10.19700/j.0379-1726.2021.03.003 (in Chinese).
Farley, K.A., Wolf, R.A., Silver, L.T., 1996. The effects of long alpha-stopping distances on (U–Th)/He ages. Geochem. Cosmochim. Acta 60 (21), 4223–4229. https://doi.org/10.1016/S0016-7037(96)00193-7.
Feng, Q.Q., Qiu, N.S., Fu, X.D., et al., 2021. Permian geothermal units in the Sichuan Basin: Implications for the thermal effect of the Emeishan mantle plume. Mar. Petrol. Geol. 132, 105226. https://doi.org/10.1016/j.marpetgeo.2021.105226.
Fjeldskaar, W., Helset, H.M., Johansen, H., et al., 2008. Thermal modelling of magmatic intrusions in the Gjallar Ridge, Norwegian Sea: Implications for vitrinite reflectance and hydrocarbon maturation. Basin Res. 20 (1), 143–159. https://doi.org/10.1111/j.1365-2117.2007.00347.x.
Flowers, R.M., Ketcham, R.A., Shuster, D.L., et al., 2009. Apatite (U–Th)/He thermochronometry using a radiation damage accumulation and annealing model. Geochem. Cosmochim. Acta 73 (8), 2347–2365. https://doi.org/10.1016/j.gca.2009.01.015.
Gao, Z.Y., Li, J.J., Zhang, B.M., et al., 2012. Identification and significance of the Middle Upper Ordovician marine source rocks in transitional zone between Awati and Manjiaer depressions, Tarim Basin. Nat. Gas. Ind. 32 (5), 5–10 (in Chinese).
Gautheron, C., Tassan-Got, L., 2010. A Monte Carlo approach to diffusion applied to noble gas/helium thermochronology. Chem. Geol. 273 (3–4), 212–224. https://doi.org/10.1016/j.chemgeo.2010.02.023.
Ginster, U., Reiners, P.W., Nasdala, L., et al., 2019. Annealing kinetics of radiation damage in zircon. Geochem. Cosmochim. Acta 249, 225–246. https://doi.org/10.1016/j.gca.2019.01.033.
Gu, Y., Wan, Y.L., Huang, J.W., et al., 2019. Ultra-deep hydrocarbon exploration prospects in the Tarim Basin under conditions of large burial depth and high pressure. Petrol. Geol. Exp. 41 (2), 157–164 (in Chinese).
Guenthner, W.R., Reiners, P.W., DeCelles, P.G., et al., 2015. Sevier belt exhumation in central Utah constrained from complex zircon (U–Th)/He data sets: Radiation damage and He inheritance effects on partially reset detrital zircons. Geol. Soc. Am. Bull. 127 (3–4), 323–348. https://doi.org/10.1130/B31032.1.
Guenthner, W.R., Reiners, P.W., Drake, H., et al., 2017. Zircon, titanite, and apatite (U–Th)/He ages and age-eU correlations from the Fennoscandian Shield, southern Sweden. Tectonics 36 (7), 1254–1274. https://doi.org/10.1002/2017TC004525.
Guenthner, W.R., Reiners, P.W., Ketcham, R.A., et al., 2013. Helium diffusion in natural zircon: Radiation damage, anisotropy, and the interpretation of zircon (U–Th)/He thermochronology. Am. J. Sci. 313 (3), 145–198. https://doi.org/10.2475/03.2013.01.
Guo, C.T., Dong, S.L., Li, Z., 2019. Detrital zircon U–Pb geochronology of the Upper Cambrian–Lower Silurian in the Wushi area, northwestern margin of Tarim Basin and its implications for provenance system and tectonic evolution. Acta Geol. Sin. 93 (11), 2759–2769 (in Chinese).
Han, J.F., Su, Z., Liu, Y.F., et al., 2018. Reservoir-controlling and pooling mechanisms and petroleum exploration potential of buried-hill belts in Yaha fault block, Tarim Basin. Acta Pet. Sin. 39 (10), 1081–1091 (in Chinese).
He, D.F., Jia, C.Z., Li, D.S., et al., 2005. Formation and evolution of polycyclic superimposed Tarim Basin. Oil Gas Geol. 26 (1), 64–77. https://doi.org/10.3321/j.issn:0253-9985.2005.01.010 (in Chinese).
He, L.J., 2022. Emeishan mantle plume and its potential impact on the Sichuan Basin: Insights from numerical modeling. Phys. Earth Planet. Inter. 323, 106841. https://doi.org/10.1016/j.pepi.2022.106841.
Hu, Y., Jia, C.Z., Chen, J.Q., et al., 2025. Restoration of hydrocarbon generation potential of the highly mature Lower Cambrian Yuertusi Formation source rocks in the Tarim Basin. Petrol. Sci. 22 (2), 588–606. https://doi.org/10.1016/j.petsci.2024.12.001.
Henkes, G.A., Passey, B.H., Grossman, E.L., et al., 2014. Temperature limits for preservation of primary calcite clumped isotope paleotemperatures. Geochem. Cosmochim. Acta 139, 362–382. https://doi.org/10.1016/j.gca.2014.04.040.
Henkes, G.A., Passey, B.H., Wanamaker Jr., A.D., et al., 2013. Carbonate clumped isotope compositions of modern marine mollusk and brachiopod shells. Geochem. Cosmochim. Acta 106, 307–325. https://doi.org/10.1016/j.gca.2012.12.020.
Huntington, K.W., Budd, D.A., Wernicke, B.P., et al., 2011. Use of clumped-isotope thermometry to constrain the crystallization temperature of diagenetic calcite. J. Sediment. Res. 81 (9), 656–669. https://doi.org/10.2110/jsr.2011.51.
Jaffrés, J.B.D., Shields, G.A., Wallmann, K., 2007. The oxygen isotope evolution of seawater: A critical review of a long-standing controversy and an improved geological water cycle model for the past 3.4 billion years. Earth Sci. Rev. 83 (1–2), 83–122. https://doi.org/10.1016/j.earscirev.2007.04.002.
Jemison Jr., R.M., 1979. Geology and development of Mills Ranch complex—World's deepest field. AAPG Bull. 63 (5), 804–809. https://doi.org/10.1306/2F9182DE-16CE-11D7-8645000102C1865D.
Jia, C.Z., Ma, D.B., Yuan, J.Y., et al., 2022. Structural characteristics, formation & evolution and genetic mechanisms of strike-slip faults in the Tarim Basin. Nat. Gas Ind. B 9 (1), 51–62. https://doi.org/10.1016/j.ngib.2021.08.017.
Jiang, X.Q., Wang, S.Y., Fan, M., et al., 2008. Study of simulation experiment for carbonate rocks dissolution in burial diagenetic environment. Petrol. Geol. Exp. 30 (6), 643–646 (in Chinese).
Johnson, J.E., Flowers, R.M., Baird, G.B., et al., 2017. "Inverted" zircon and apatite (U–Th)/He dates from the Front Range, Colorado: High-damage zircon as a low-temperature (<50 °C) thermochronometer. Earth Planet Sci. Lett. 466, 80–90. https://doi.org/10.1016/j.epsl.2017.03.002.
Ketcham, R.A., 2005. Forward and inverse modeling of low-temperature thermochronometry data. Rev. Mineral. Geochem. 58 (1), 275–314. https://doi.org/10.2138/rmg.2005.58.11.
Kim, S.T., Coplen, T.B., Horita, J., 2015. Normalization of stable isotope data for carbonate minerals: Implementation of IUPAC guidelines. Geochem. Cosmochim. Acta 158, 276–289. https://doi.org/10.1016/j.gca.2015.02.011.
Li, D., Chang, J., Qiu, N.S., et al., 2022. The thermal history in sedimentary basins: A case study of the central Tarim Basin, Western China. J. Asian Earth Sci. 229, 105149. https://doi.org/10.1016/j.jseaes.2022.105149.
Li, H.L., Ma, A.L., Cai, X.Y., et al., 2021. Kinetics of oil-cracking of ultra-deep Ordovician oil in the North Shuntuoguole area of Tarim Basin and its geological implications. Petrol. Geol. Exp. 43 (5), 818–825. https://doi.org/10.11781/sysydz202105818 (in Chinese).
Li, H.L., Qiu, N.S., Jin, Z.J., et al., 2005. Geothermal history in the Tarim Basin. West China Petrol. Geosci. 1 (1), 15–18 (in Chinese).
Li, J., Zhou, X., Li, W., et al., 2015. Preliminary reconstruction of tectonic paleogeography of Tarim Basin and its adjacent areas from Cambrian to Triassic, NW China. Geol. Rev. 61 (6), 1225–1234 (in Chinese).
Li, J.W., Li, Z., Qiu, N.S., et al., 2016. Carboniferous–Permian abnormal thermal evolution of the Tarim Basin and its implication for deep structure and magmatic activity. Chin. J. Geophys. 59 (9), 3318–3329. https://doi.org/10.6038/cjg20160916 (in Chinese).
Li, M.J., Wang, T.G., Chen, J.F., et al., 2010. Paleo-heat flow evolution of the Tabei Uplift in Tarim Basin, northwest China. J. Asian Earth Sci. 37 (1), 52–66. https://doi.org/10.1016/j.jseaes.2009.07.007.
Li, Y.J., Yang, H.J., Zhang, G.Y., et al., 2012. Redivision of the tectonic units of Tabei Rise in Tarim Basin, NW China. Acta Pet. Sin. 28 (8), 2466–2478 (in Chinese).
Lin, C., Yang, H., Liu, J., et al., 2012. Distribution and erosion of the Paleozoic tectonic unconformities in the Tarim Basin, Northwest China: Significance for the evolution of paleo-uplifts and tectonic geography during deformation. J. Asian Earth Sci. 46, 1–19. https://doi.org/10.1016/j.jseaes.2011.10.004.
Liu, C.L., Zhang, Y.Q., Zhang, Y., et al., 2018. Analysis of regional structural cross section of the North and Central Tarim Basin and new insights into paleo-uplift origin. Oil Gas Geol. 39 (5), 1001–1010. https://doi.org/10.11743/ogg20180514 (in Chinese).
Liu, H.Q., Xu, Y.G., Tian, W., et al., 2014. Origin of two types of rhyolites in the Tarim Large Igneous Province: Consequences of incubation and melting of a mantle plume. Lithos 204, 59–72. https://doi.org/10.1016/j.lithos.2014.02.007.
Liu, J.L., Jiang, Z.X., Liu, K.Y., et al., 2015. Hydrocarbon accumulation process of the Yaha tectonic belt, Kuqa foreland basin. Nat. Gas Geosci. 26 (1), 43–53 (in Chinese).
Liu, Y.C., Qiu, N.S., Chang, J., et al., 2020. Application of clumped isotope thermometry to thermal evolution of sedimentary basins: A case study of Shuntuoguole area in Tarim Basin. Chin. J. Geophys. 63 (2), 597–611 (in Chinese). https://doi.org/10.6038/cjg2020N0152.
Liu, Y., Yang, C.Y., Xiao, D.Q., et al., 2017. Hydrocarbon phase limit and conversion process in the deep formation of rift lacustrine basin from Qikou Sag of Bohai Bay Basin, eastern China. Nat. Gas Geosci. 28 (5), 703–712. https://doi.org/10.11764/j.issn.1672-1926.2017.04.001 (in Chinese).
Liu, Y.L., Hu, X.F., Huang, Z.B., et al., 2012. $^{40}Ar/^{39}Ar$ geochronology and geochemistry of the volcanic rocks from the west segment of Tabei uplift, Tarim Basin. Acta Pet. Sin. 28 (8), 2423–2434 (in Chinese).
Lloyd, M.K., Eiler, J.M., Nabelek, P.I., 2017. Clumped isotope thermometry of calcite and dolomite in a contact metamorphic environment. Geochem. Cosmochim. Acta 197, 323–344. https://doi.org/10.1016/j.gca.2016.10.037.
Lloyd, M.K., Ryb, U., Eiler, J.M., 2018. Experimental calibration of clumped isotope reordering in dolomite. Geochem. Cosmochim. Acta 242, 1–20. https://doi.org/10.1016/j.gca.2018.08.036.
Lü, X.X., Zhou, X.Y., Li, J.J., et al., 2007. Hydrocarbon accumulation characteristics of the carbonate rock in the northern uplift of the Tarim Basin. Acta Geol. Sin. 81 (8), 1057–1064. https://doi.org/10.3321/j.issn:0001-5717.2007.08.005 (in Chinese).
Ma, A., 2016. Kinetics of oil-cracking for different types of marine oils from Tahe Oilfield, Tarim Basin, NW China. J. Nat. Gas Geosci. 1 (1), 35–43. https://doi.org/10.1016/j.jngs.2016.03.001.
Ma, Y., Cai, X., Yun, L., et al., 2022. Practice and theoretical and technical progress in exploration and development of Shunbei ultra-deep carbonate oil and gas field, Tarim Basin, NW China. Petrol. Explor. Dev. 49 (1), 1–20. https://doi.org/10.1016/S1876-3804(22)60001-6.

Mangenot, X., Deçoninck, J.F., Bonifacie, M., et al., 2019. Thermal and exhumation histories of the northern subalpine chains (bauges and Bornes—France): Evidence from forward thermal modeling coupling clay mineral diagenesis, organic maturity and carbonate clumped isotope (Δ_{47}) data. Basin Res. 31 (2), 361–379. https://doi.org/10.1111/bre.12324.

Mao, Q.Y., Zhu, D.P., Lü, H.T., et al., 2014. Hydrocarbon enrichment rule in northern Tarim Basin. Inner Mongolia Petrochemical Industry 40 (5), 145–148 (in Chinese).

Meng, X.X., Wang, H.B., Yao, Q.Z., et al., 2015. Tectonic evolution characteristics of Tabei Uplift and its controlling effect on the reservoir and hydrocarbon accumulation of Ordovician carbonate. Nat. Gas Geosci. 26 (S1), 109–120 (in Chinese).

Müller, I.A., Rodriguez-Blanco, J.D., Storck, J.C., et al., 2019. Calibration of the oxygen and clumped isotope thermometers for (proto-)dolomite based on synthetic and natural carbonates. Chem. Geol. 525, 1–17. https://doi.org/10.1016/j.chemgeo.2019.07.014.

Müller, I.A., Violay, M.E.S., Storck, J.C., et al., 2017. Clumped isotope fractionation during phosphoric acid digestion of carbonates at 70 °C. Chem. Geol. 449, 1–14. https://doi.org/10.1016/j.chemgeo.2016.11.030.

Naylor, H.N., Defliese, W.F., Grossman, E.L., et al., 2020. Investigation of the thermal history of the Delaware Basin (West Texas, USA) using carbonate clumped isotope thermometry. Basin Res. 32 (5), 1140–1155. https://doi.org/10.1111/bre.12419.

Ni, Z.Y., Wang, T.G., Li, M.J., et al., 2016. An examination of the fluid inclusions of the well RP3-1 at the Halahatang Sag in Tarim Basin, northwest China: Implications for hydrocarbon charging time and fluid evolution. J. Petrol. Sci. Eng. 146, 326–339. https://doi.org/10.1016/j.petrol.2016.04.038.

O'Neil, J.R., Clayton, R.N., Mayeda, T.K., 1969. Oxygen isotope fractionation in divalent metal carbonates. J. Chem. Phys. 51 (12), 5547–5558. https://doi.org/10.1063/1.1671982.

Orme, D.A., Guenthner, W.R., Laskowski, A.K., et al., 2016. Long-term tectonothermal history of Laramide basement from zircon–He age-eU correlations. Earth Planet Sci. Lett. 453, 119–130. https://doi.org/10.1016/j.epsl.2016.07.046.

Passey, B.H., Henkes, G.A., 2012. Carbonate clumped isotope bond reordering and geospeedometry. Earth Planet Sci. Lett. 351–352, 223–236. https://doi.org/10.1016/j.epsl.2012.07.021.

Passey, B.H., Levin, N.E., Cerling, T.E., et al., 2010. High-temperature environments of human evolution in East Africa based on bond ordering in paleosol carbonates. Proc Natl Acad Sci USA 107 (25), 11245–11249. https://doi.org/10.1073/pnas.1001824107.

Peng, J., Wang, X., Han, H., et al., 2018. Simulation for the dissolution mechanism of Cambrian carbonate rocks in Tarim Basin, NW China. Petrol. Explor. Dev. 45 (3), 431–441. https://doi.org/10.1016/S1876-3804(18)30048-X.

Pepper, A.S., Dodd, T.A., 1995. Simple kinetic models of petroleum formation. Part II: Oil-gas cracking. Mar. Petrol. Geol. 12 (3), 321–340. https://doi.org/10.1016/0264-8172(95)98382-F.

Petersen, S.V., Defliese, W.F., Saenger, C., et al., 2019. Effects of improved ^{17}O correction on interlaboratory agreement in clumped isotope calibrations, estimates of mineral-specific offsets, and temperature dependence of acid digestion fractionation. G-cubed 20 (7), 3495–3519. https://doi.org/10.1029/2018GC008127.

Powell, J., Schneider, D., Stockli, D., et al., 2016. Zircon (U–Th)/He thermochronology of Neoproterozoic strata from the Mackenzie Mountains, Canada: Implications for the Phanerozoic exhumation and deformation history of the northern Canadian Cordillera. Tectonics 35 (3), 663–689. https://doi.org/10.1002/2015TC003989.

Qi, Y.A., Liu, G.Q., 1999. Wave process analysis of sedimentary basin and erosion quantity of unconformities. J. Jiaozuo Inst. Technol. 18 (3), 161–165. https://doi.org/10.3969/j.issn.1673-9787.1999.03.002.

Qiao, Z.F., Zhang, S.N., Shen, A.J., et al., 2020. Laser ablated U–Pb dating-based determination of burial dolomitization process: A case study of Lower Ordovician Penglaiba Formation of Yonganba Outcrop in Tarim Basin. Acta Pet. Sin. 36 (11), 3493–3509. https://doi.org/10.18654/1000-0569/2020.11.15 (in Chinese).

Qing, H.R., Veizer, J., 1994. Oxygen and carbon isotopic composition of Ordovician brachiopods: Implications for coeval seawater. Geochem. Cosmochim. Acta 58 (20), 4429–4442. https://doi.org/10.1016/0016-7037(94)90345-X.

Qiu, N.S., Chang, J., Zuo, Y.H., et al., 2012. Thermal evolution and maturation of lower Paleozoic source rocks in the Tarim Basin, northwest China. AAPG Bull. 96 (5), 789–821. https://doi.org/10.1306/09071111029.

Qiu, N.S., Jin, Z.J., Wang, F.Y., 1997. The effect of the complex geothermal field based on the multi-structure evolution to hydrocarbon generation—A case of Tazhong area in Tarim Basin. Acta Sedimentol. Sin. 15 (2), 142–144 (in Chinese).

Qiu, N.S., Liu, W., Xu, Q.C., et al., 2018. Temperature–pressure field and hydrocarbon accumulation in deep-ancient marine strata. Earth Sci. 43 (10), 3511–3525 (in Chinese).

Qiu, N.S., Reiners, P., Mei, Q.H., et al., 2009. Application of the (U–Th)/He thermochronometry to the tectono-thermal evolution of sedimentary basin: A case history of Well KQ1 in the Tarim Basin. Chin. J. Geophys. 52 (4), 803–813. https://doi.org/10.1002/cjg2.1403.

Qiu, N.S., Wang, J.Y., Mei, Q.H., et al., 2010. Constraints of (U–Th)/He ages on early Paleozoic tectonothermal evolution of the Tarim Basin, China. Sci. China Earth Sci. 53 (7), 964–976. https://doi.org/10.1007/s11430-010-4004-1.

Quigley, T.M., MacKenzie, A.S., 1988. The temperatures of oil and gas formation in the sub-surface. Nature 333 (6173), 549–552. https://doi.org/10.1038/333549a0.

Rasbury, E.T., Cole, J.M., 2009. Directly dating geologic events: U–Pb dating of carbonates. Rev. Geophys. 47 (3), RG3001. https://doi.org/10.1029/2007RG000246.

Reiners, P.W., Spell, T.L., Nicolescu, S., et al., 2004. Zircon (U–Th)/He thermochronometry: He diffusion and comparisons with $^{40}Ar/^{39}Ar$ dating. Geochem. Cosmochim. Acta 68 (8), 1857–1887. https://doi.org/10.1016/j.gca.2003.10.021.

Ren, Z.L., Cui, J.P., Qi, K., et al., 2020. Control effects of temperature and thermal evolution history of deep and ultra-deep layers on hydrocarbon phase state and hydrocarbon generation history. Nat. Gas. Ind. 40 (2), 22–30. https://doi.org/10.3787/j.issn.1000-0976.2020.02.003 (in Chinese).

Ren, Z.L., Xiao, H., Han, W., et al., 2009. Research on basin-mountain tectonic-thermal history of Kongquehe Slope and Kuruketag Uplift. J. Northwest Univ. Nat. Sci. Ed. 39 (3), 510–516 (in Chinese).

Roberts, N.M.W., Rasbury, E.T., Parrish, R.R., et al., 2017. A calcite reference material for LA-ICP-MS U–Pb geochronology. G-cubed 18 (7), 2807–2814. https://doi.org/10.1002/2016GC006784.

Ryb, U., Eiler, J.M., 2018. Oxygen isotope composition of the Phanerozoic ocean and a possible solution to the dolomite problem. Proc Natl Acad Sci USA 115 (26), 6602–6607. https://doi.org/10.1073/pnas.1719681115.

Shen, A.J., Wang, Z.M., Zheng, X.P., et al., 2007. Genesis classification and characteristics of Cambrian–Ordovician carbonate reservoirs and petroleum exploration potential in Yaka-Yengimahalla area, Tarim Basin. Mar. Origin Petrol. Geol. 12 (2), 23–32. https://doi.org/10.3969/j.issn.1672-9854.2007.02.004 (in Chinese).

Shi, K.B., Liu, B., Jiang, W.M., et al., 2018. Nanhua–Sinian tectono-sedimentary framework of Tarim Basin, NW China. Oil Gas Geol. 39 (5), 862–877 (in Chinese).

Slater, B.E., Smith, L.B., 2012. Outcrop analog for Trenton–Black River hydrothermal dolomite reservoirs, Mohawk Valley, New York. AAPG Bull. 96 (7), 1369–1388. https://doi.org/10.1306/10041110200.

Stewart, A.K., Massey, M., Padgett, P.L., et al., 2005. Influence of a basic intrusion on the vitrinite reflectance and chemistry of the Springfield (No. 5) coal, Harrisburg, Illinois. Int. J. Coal Geol. 63 (1–2), 58–67. https://doi.org/10.1016/j.coal.2005.02.005.

Stolper, D.A., Eiler, J.M., 2015. The kinetics of solid-state isotope-exchange reactions for clumped isotopes: A study of inorganic calcites and apatites from natural and experimental samples. Am. J. Sci. 315 (5), 363–411. https://doi.org/10.2475/05.2015.01.

Su, J., Zhang, S.C., Yang, H.J., et al., 2011. Evidence of the organic geochemistry and petrology for the adjustment process of primary reservoir: Insight into the adjustment mechanism of Hadexun oil field visa Xiang-3 well. Acta Pet. Sin. 27 (6), 1886–1898 (in Chinese).

Sun, D.S., Li, S.J., Li, J.J., et al., 2022. Insights from a comparison of hydrocarbon accumulation conditions of Sinian–Cambrian between the Tarim and the Sichuan basins. Acta Geol. Sin. 96 (1), 249–264. https://doi.org/10.3969/j.issn.0001-5717.2022.01.020 (in Chinese).

Tian, H., Wang, Z., Xiao, Z., et al., 2006. Oil cracking to gases: Kinetic modeling and geological significance. Chin. Sci. Bull. 51 (22), 2763–2770. https://doi.org/10.1007/s11434-006-2188-8.

Tian, W., Campbell, I.H., Allen, C.M., et al., 2010. The Tarim picrite–basalt–rhyolite suite, a Permian flood basalt from northwest China with contrasting rhyolites produced by fractional crystallization and anatexis. Contrib. Mineral. Petrol. 160 (3), 407–425. https://doi.org/10.1007/S00410-009-0485-3.

Veillard, C.M.A., John, C.M., Krevor, S., et al., 2019. Rock-buffered recrystallization of Marion Plateau dolomites at low temperature evidenced by clumped isotope thermometry and X-ray diffraction analysis. Geochem. Cosmochim. Acta 252, 190–212. https://doi.org/10.1016/j.gca.2019.02.012.

Veizer, J., Prokoph, A., 2015. Temperatures and oxygen isotopic composition of Phanerozoic oceans. Earth Sci. Rev. 146, 92–104. https://doi.org/10.1016/j.earscirev.2015.03.008.

Vermeesch, P., 2018. IsoplotR: A free and open toolbox for geochronology. Geosci. Front. 9 (5), 1479–1493. https://doi.org/10.1016/j.gsf.2018.04.001.

Wadleigh, M.A., Veizer, J., 1992. $^{18}O/^{16}O$ and $^{13}C/^{12}C$ in lower Paleozoic articulate brachiopods: Implications for the isotopic iomposition of seawater. Geochem. Cosmochim. Acta 56 (1), 431–443. https://doi.org/10.1016/0016-7037(92)90143-7.

Wang, H.H., 2019. Formation and controlling factors of effective weathered crust carbonate reservoirs—taking the Yingmaili-Yaha area of Tarim Basin as an example. IOP Conf. Ser. Mater. Sci. Eng. 585 (1), 012082. https://doi.org/10.1088/1757-899X/585/1/012082.

Wang, T.G., Dai, S.F., Li, M.J., et al., 2010. Stratigraphic thermohistory and its implications for regional geoevolution in the Tarim Basin, NW China. Sci. China Earth Sci. 53 (10), 1495–1505. https://doi.org/10.1007/s11430-010-4069-x.

Waples, D.W., 2000. The kinetics of in-reservoir oil destruction and gas formation: Constraints from experimental and empirical data, and from thermodynamics. Org. Geochem. 31 (6), 553–575. https://doi.org/10.1016/S0146-6380(00)00023-1.

Woodhead, J.D., Hergt, J.M., 2001. A preliminary appraisal of seven natural glasses as reference materials for in situ microanalysis. Geostand. Newsl. 25 (2–3), 261–286. https://doi.org/10.1111/j.1751-908X.2001.tb00600.x.

Wu, G.K., Lin, C.S., Liu, Y.F., et al., 2019. Characteristics of major unconformities and paleo-geomorphology during the Mesozoic key transformation stages in Kuqa-

Tabei area. Oil Gas Geol. 40 (4), 763–777. https://doi.org/10.11743/ogg20190407 (in Chinese).
Xiao, W.J., Windley, B.F., Huang, B.C., et al., 2009. End-Permian to mid-triassic termination of the accretionary processes of the southern Altaids: Implications for the geodynamic evolution, Phanerozoic continental growth, and metallogeny of Central Asia. Int. J. Earth Sci. 98 (6), 1189–1217. https://doi.org/10.1007/s00531-008-0407-z.
Xu, Y.G., Wei, X., Luo, Z.Y., et al., 2014. The Early Permian Tarim Large Igneous Province: Main characteristics and a plume incubation model. Lithos 204, 20–35. https://doi.org/10.1016/j.lithos.2014.02.015.
Xu, Z.Q., He, B.Z., Zhang, C.L., et al., 2013. Tectonic framework and crustal evolution of the Precambrian basement of the Tarim Block in NW China: New geochronological evidence from deep drilling samples. Precambr. Res. 235, 150–162. https://doi.org/10.1016/j.precamres.2013.06.001.
Yang, H.J., Chen, Y.Q., Tian, J., et al., 2020a. Great discovery and its significance of ultra-deep oil and gas exploration in well Luntan-1 of the Tarim Basin. China Petrol. Explor 25 (2), 62–72. https://doi.org/10.3969/j.issn.1672-7703.2020.02.007 (in Chinese).
Yang, H.J., Yu, S., Zhang, H.Z., et al., 2020b. Geochemical characteristics of Lower Cambrian sources rocks from the deepest drilling of well LT-1 and their significance to deep oil gas exploration of the Lower Paleozoic system in the Tarim Basin. Geochimica 49 (6), 666–682. https://doi.org/10.19700/j.0379-1726.2021.01.017 (in Chinese).
Yang, P., Wu, G., Nuriel, P., et al., 2021. In situ LA-ICPMS U–Pb dating and geochemical characterization of fault-zone calcite in the central Tarim Basin, northwest China: Implications for fluid circulation and fault reactivation. Chem. Geol. 568, 120125. https://doi.org/10.1016/j.chemgeo.2021.120125.
Yang, S.F., Chen, H.L., Li, Z.L., et al., 2013. Early Permian tarim large igneous Province in northwest China. Sci. China Earth Sci. 56 (12), 2015–2026. https://doi.org/10.1007/s11430-013-4653-y.
Yang, X., Li, H.L., Yue, Y., et al., 2017. The strata and palaeo-geomorphology framework at the end of Neoproterozoic and development mode of source rocks at the beginning of Cambrian in Tarim Basin, China. J. Nat. Gas Geosci. 2 (5–6), 313–322. https://doi.org/10.1016/j.jnggs.2018.02.003.
Yun, L., 2021. Hydrocarbon accumulation of ultra-deep Ordovician fault-karst reservoirs in Shunbei area. Xinjing Pet. Geol. 42 (2), 136–142. https://doi.org/10.7657/XJPG20210202 (in Chinese).
Zhang, C.J., Jia, C.Z., Li, B.L., et al., 2010a. Ancient karsts and hydrocarbon accumulation in the middle and western parts of the North Tarim uplift, NW China. Petrol. Explor. Dev. 37 (3), 263–269. https://doi.org/10.1016/S1876-3804(10)60032-8.
Zhang, D., Zhang, Z., Mao, J., et al., 2016. Zircon U–Pb ages and Hf–O isotopic signatures of the Wajilitag and Puchang Fe–Ti oxide-bearing intrusive complexes: Constraints on their source characteristics and temporal–spatial evolution of the Tarim Large Igneous Province. Gondwana Res. 37, 71–85. https://doi.org/10.1016/j.gr.2016.05.011.
Zhang, D., Zhang, Z., Santosh, M., et al., 2013. Perovskite and baddeleyite from kimberlitic intrusions in the Tarim large igneous province signal the onset of an end-carboniferous mantle plume. Earth Planet Sci. Lett. 361, 238–248. https://doi.org/10.1016/j.epsl.2012.10.034.
Zhang, N.C., Cui, H.F., Teng, T.Y., et al., 2010b. Features of carbonate buried hill oil and gas reservoir in Yingmaili-Yaha region, Tarim Basin. Nat. Gas Geosci. 21 (5), 762–771 (in Chinese).
Zhang, Y., Munnecke, A., 2016. Ordovician stable carbon isotope stratigraphy in the Tarim Basin, NW China. Palaeogeogr. Palaeoclimatol. Palaeoecol. 458, 154–175. https://doi.org/10.1016/j.palaeo.2015.09.001.
Zhang, Y.W., Jin, Z.J., Liu, G.C., et al., 2000. Study on the formation of unconformities and the amount of eroded sedimentation in Tarim Basin. Earth Sci. Front. 7 (4), 449–457 (in Chinese).
Zhong, C., Shi, H., Tang, X.Y., et al., 2024. Reconstruction of the thermal evolution since the Late Paleozoic in the Ounan Sag, eastern Qaidam Basin, NW China: New constraints from vitrinite reflectance data and (U–Th)/He thermochronology. Petrol. Sci. 21 (5), 2984–3000. https://doi.org/10.1016/j.petsci.2024.05.011.
Zhu, G., Milkov, A.V., Li, J., et al., 2021. Deepest oil in Asia: Characteristics of petroleum system in the Tarim Basin, China. J. Petrol. Sci. Eng. 199, 108246. https://doi.org/10.1016/j.petrol.2020.108246.
Zhu, G.Y., Liu, X.W., Zhu, Y.F., et al., 2013. The characteristics and the accumulation mechanism of complex reservoirs in the Hanilcatam area, Tarim Basin. Bull. China Soc. Mineral Petrol. Geochem. 32 (2), 231–242. https://doi.org/10.3969/j.issn.1007-2802.2013.02.009 (in Chinese).